

Intrinsic First and Higher-Order Topological Superconductivity in a Doped Topological Insulator

Harley Scammell (✉ h.scammell@unsw.edu.au)

The University of New South Wales

Julian Ingham

Boston University

Max Geier

Freie Universität Berlin <https://orcid.org/0000-0002-7552-5763>

Tommy Li

Freie Universität Berlin

Article

Keywords: topological, superconductivity, diagonalisation, heterostructure

Posted Date: September 27th, 2021

DOI: <https://doi.org/10.21203/rs.3.rs-899707/v1>

License: © ⓘ This work is licensed under a Creative Commons Attribution 4.0 International License.

[Read Full License](#)

Intrinsic first and higher-order topological superconductivity in a doped topological insulator

Harley D. Scammell,^{1,2,*} Julian Ingham,³ Max Geier,^{4,5} and Tommy Li⁴

¹*School of Physics, University of New South Wales, Sydney 2052, Australia*

²*Australian Research Council Centre of Excellence in Future Low-Energy Electronics Technologies, University of New South Wales, Sydney 2052, Australia*

³*Physics Department, Boston University, Commonwealth Avenue, Boston, MA 02215, USA*

⁴*Dahlem Center for Complex Quantum Systems and Fachbereich Physik, Freie Universität Berlin, Arnimallee 14, 14195 Berlin, Germany*

⁵*Center for Quantum Devices, Niels Bohr Institute, University of Copenhagen, DK-2100 Copenhagen, Denmark*

(Dated: September 12, 2021)

We explore higher-order topological superconductivity in an artificial Dirac material with intrinsic spin-orbit coupling. A mechanism for superconductivity due to repulsive interactions – *pseudospin pairing* – has recently been shown to result in higher-order topology in Dirac systems past a minimum chemical potential [1]. Here we apply this theory through microscopic modelling of a superlattice potential imposed on an inversion symmetric hole-doped semiconductor heterostructure, and extend previous work to include the effects of spin-orbit coupling. We find spin-orbit coupling enhances interaction effects, providing an experimental handle to increase the efficiency of the superconducting mechanism. We find that the phase diagram, as a function of chemical potential and interaction strength, contains three superconducting states – a first-order topological $p+ip$ state, a second-order topological spatially modulated $p+i\tau p$ state, and a second-order topological extended s -wave state, s_τ . We calculate the symmetry-based indicators for the $p+i\tau p$ and s_τ states, which prove these states possess second-order topology. Exact diagonalisation results are presented which illustrate the interplay between the boundary physics and spin orbit interaction. We argue that this class of systems offer an experimental platform to engineer and explore first and higher-order topological superconducting states.

CONTENTS

11		22	VI. Competing Instabilities	10
12	I. Introduction	2	VII. Topological properties of the superconducting phases	11
13	II. Single particle effective Hamiltonian	3	A. Symmetry-based indicators for $p+i\tau p$ and s_τ phases	12
14	A. Spin-orbit coupled honeycomb superlattice	3	B. Exact diagonalisation results	14
15	B. Effective Dirac Hamiltonian	4	VIII. Discussion	16
16	III. Coulomb Matrix Elements	5	Acknowledgements	17
17	IV. Screening	5	References	17
18	V. Superconducting instabilities	6	A. Deriving the Effective Hamiltonian	21
19	A. Interactions in the Cooper channel	6	1. Superlattice potential	21
20	B. Gap equation	7	2. Effective Dirac Hamiltonian	21
21	C. Explicit solution and phase diagram	8	B. Polarization Operators	23
		32	1. Preliminaries	23
		33	2. Results	23
		34		

* h.scammell@unsw.edu.au

35 C. Interactions in Cooper channel

36 D. Effective tight-binding model for the superlattice

37 E. The pairing term in the lattice representation

38 a. s_τ

39 b. $p + ip$

40 c. $p + i\tau p$

41 I. INTRODUCTION

42 Higher-order topological superconductors are superconducting
43 phases which exhibit gapless corner (hinge) modes in two (three)
44 dimensions protected by spatial symmetries and the bulk gap, and
45 have recently attracted immense interest [2–29]. It was recently pro-
46 posed that Dirac materials, with purely repulsive interactions and
47 sufficiently localised orbitals, intrinsically give rise to higher-order
48 topological superconductivity [1]. We will refer to this as mecha-
49 nism as *pseudospin pairing*.

50 Superlattices are a promising platform for this mechanism [30],
51 since they allow the experimental study of materials with tunable
52 lattice constants, atomic orbitals and interactions [31], and have been
53 extensively explored in the context of optical lattices [32–35] and van
54 der Waals heterostructures [36–42]. Recently, significant experimen-
55 tal progress has also been made in forming honeycomb superlattices
56 in patterned semiconductor heterostructures [43–48]. Motivated by
57 these developments, in this paper we discuss a p -type quantum well
58 overlaid with a periodic potential with honeycomb symmetry (see
59 e.g. Refs [49–53]) as an explicit realisation of the pseudospin pairing
60 mechanism. Here we extend the theory to include the influence of
61 intrinsic spin-orbit coupling. The superlattice potential gives rise to
62 Dirac band crossings at the K, K' points; accounting for the intrinsic
63 spin-orbit coupling gives rise to a spin-dependent mass for the Dirac
64 fermions, opening up a \mathbb{Z}_2 topological bandgap. The low energy
65 effective theory is equivalent to the Kane–Mele model for a topolog-
66 ical insulator [52–54], with an effective Dirac velocity controlled by
67 the strength of spin-orbit coupling. We find that spin-orbit coupling
68 enhances the superconducting instability and provides an additional
69 handle to manipulate the topological superconducting phases.

70 We present results specifically for a model of an artificial honey-
71 comb lattice based on a nanopatterned hole-doped semiconductor
72 quantum well, having in mind the fact that in this situation there
73 is a high degree of experimental control over the electron-electron
74 interaction as well as the band structure. However, our field theory

26 treatment is generic and we anticipate our the results are relevant to
76 a number of other Dirac materials, in which similar spin-orbit physics
27 is present alongside localised orbitals. Unconventional superconduc-
78 tivity has recently been observed in twisted transition metal dichalo-
29 genides (TMDs) [55], which are Dirac systems where spin-orbit cou-
30 pling plays an important role. Theoretical studies of twisted TMDs,
31 e.g. Ref. [56], have suggested effective models for the superlattice
32 potential similar to the one we examine in the present paper. Su-
33 perconductivity has also been seen in the intrinsic heterostructure
34 $\text{Ba}_6\text{Nb}_{11}\text{S}_{28}$, a material which can be modelled as a stack of decou-
35 pled NbS_2 layers subjected to a superlattice potential arising from
36 the Ba_3NbS_5 spacer layers [57]. Other than superlattice systems,
37 superconductivity is seen in spin-orbit coupled topological materials
38 including $\text{Pb}_{1/3}\text{TaS}_2$ [58], few-layer stanene [59], monolayer TMDs
39 [60–64], doped topological insulators [65–73], and recently discovered
40 vanadium-based kagome metals [74–93].

41 We determine the phase diagram of the system as a function of
42 chemical potential and interaction strength. Employing physically
43 realistic parameters, we find three adjacent superconducting phases
44 – one first-order topological $p + ip$ intervalley, and two higher-order
45 topological: s_τ intervalley, and $p + i\tau p$ intravalley – with spin-orbit
46 coupling entangling the valley and spin polarisation of the Cooper
47 pairs. The s_τ state is similar to the s_\pm state discussed in the context
48 of iron-based superconductors, which consists of s -wave pairing but
49 with a gap that has opposite signs at the hole and electron pockets
50 [94–99]; here, the valley structure imposes that s -wave state changes
51 sign under exchange of the valleys.

52 The $p + i\tau p$ and s_τ pairing instabilities satisfy a simple criterion for
53 second-order topology derived from symmetry-based indicators [5–
54 7]: by counting the inversion eigenvalues of the valence and conduc-
55 tion bands in the normal state, we prove that if a superconducting
56 instability with odd inversion parity opens a full excitation gap in a
57 hole-doped Kane–Mele honeycomb system, then the resulting super-
58 conducting state must have second-order topology, hosting Kramers
59 pairs of Majorana corner modes. This conclusion holds for weak
60 spin-orbit coupling much smaller than the bandwidth, and for the
61 onset of superconductivity where the superconducting order param-
62 eter is the smallest energy scale. The second-order topological phase
63 persists as long as increasing the superconducting order parameter
64 does not close the bulk excitation gap.

65 In Section II, we will outline how the effective Dirac theory arises
66 from the superlattice imposed on the 2D hole gas. In Section III, we
67 will discuss the form of the symmetry-allowed interactions for the

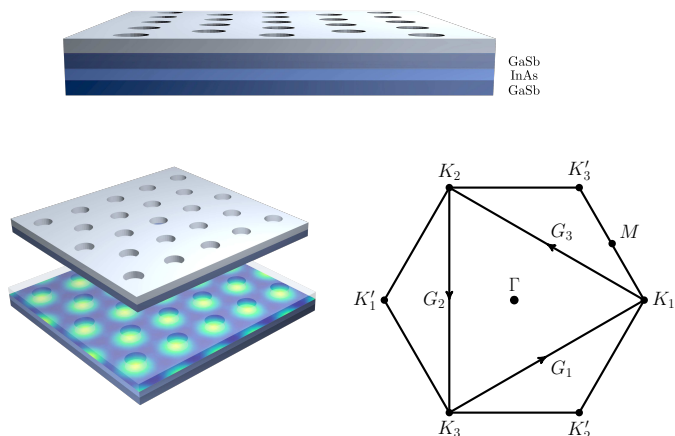


FIG. 1: Schematic view of the honeycomb superlattice patterned on the heterostructure 2DHG – a patterned dielectric or gate is placed on a quantum well e.g. GaSb-InAs-GaSb. Superlattice Brillouin zone: the reciprocal lattice vectors \mathbf{G}_i connect zone corners corresponding to \mathbf{K}_j , and connect corners corresponding to \mathbf{K}'_j , the parity reflections of \mathbf{K}_j .

effective Dirac system. Particularly important are the pseudospin-dependent Hubbard interactions; we present numerical results for these parameters based on explicit calculations. In Section IV, we will analyse the screening properties of this system – screening plays a crucial role for superconducting pairing mechanism, as discussed in the earlier work (for electrons, without spin-orbit coupling [30]). It was shown that the pseudospin-dependent Hubbard interactions are antiscreened (enhanced) by many-body effects; we analyse this phenomenon in the presence of spin-orbit coupling. In Section V, we present the solution to the BCS gap equation using the screened form of the interactions, and present a phase diagram of possible superconducting states. In Section VII, we discuss the phenomenology of the possible superconducting phases, and present numerical results describing the edge physics as well as symmetry indicators which confirm the higher topology of the $p + i\tau p$ and s_τ states.

II. SINGLE PARTICLE EFFECTIVE HAMILTONIAN

In this section, we will present the effective Dirac theory that arises for a particular honeycomb superlattice system – p -type artificial graphene – though aspects of the model apply generally. We briefly outline the schematics of artificial graphene, and in doing so establish the key parameters which may be tuned in experiment.

A. Spin-orbit coupled honeycomb superlattice

We consider a p -type quantum well, having in mind for e.g. a GaSb-InAs-GaSb heterojunction (see Fig. 1). The hole gas experiences a potential well, arising from the band-bending along the growth direction of the heterojunction, confining the holes along the z -direction leaving a two dimensional hole gas (2DHG) unconfined in the xy plane. The hole states are formed from $p_{\frac{3}{2}}$ orbitals and can be described by the Luttinger Hamiltonian involving spin- $\frac{3}{2}$ operators \mathbf{S} in the axial approximation, i.e. $U(1)$ symmetry in-plane [100]. Ignoring the cubic anisotropy of the zincblende lattice, which has a weak effect for the carrier densities we consider, the Hamiltonian is

$$H_{2DHG} = \frac{1}{2m_e} \left[(\gamma_1 + \frac{5}{2}\gamma_2)\mathbf{p}^2 - 2\gamma_2(\mathbf{p} \cdot \mathbf{S})^2 \right] + W_c(z) \quad (1)$$

The γ_i are the Luttinger parameters; in what follows we shall use parameters for InAs, presented in Table I. In this work we model the confinement as a rectangular infinite well of width d ,

$$W_c(z) = \begin{cases} 0, & z \in (-d/2, d/2) \\ \infty, & \text{otherwise.} \end{cases} \quad (2)$$

The Hamiltonian (1) satisfies time-reversal and inversion symmetry, so each 2D subband is twofold degenerate. We consider densities for which only the lowest pair of subbands is occupied, and introduce an effective spin- $\frac{1}{2}$ degree of freedom with Pauli matrices s_μ .

Next, we consider the influence of a periodic electrostatic potential, with honeycomb symmetry, on the 2DHG, i.e. the superlattice. Experimentally, this may be implemented by etching the pattern onto a metal plate or dielectric on top of the 2DHG. A minimal model of the superlattice is given by [49],

$$W(\mathbf{r}) = 2W_0 \sum_i \cos(\mathbf{G}_i \cdot \mathbf{r}), \quad (3)$$

where $\mathbf{G}_1 = \mathbf{K}_2 - \mathbf{K}_1$, $\mathbf{G}_2 = \mathbf{K}_3 - \mathbf{K}_2$, $\mathbf{G}_3 = \mathbf{K}_1 - \mathbf{K}_3$; $\mathbf{K}_1 = \frac{4\pi}{3L}(1, 0)$, $\mathbf{K}_2 = \frac{4\pi}{3L}\frac{1}{2}(-1, \sqrt{3})$, $\mathbf{K}_3 = \frac{4\pi}{3L}\frac{1}{2}(-1, -\sqrt{3})$, with (super)-lattice constant L , and magnitude of the electrostatic potential W_0 .

TABLE I: Physical parameters for InAs.

Parameter	Details	Value
γ_1	Luttinger parameter	20.4
γ_2	Luttinger parameter	8.3
γ_3	Luttinger parameter	9.1
m_H	Effective mass: $m_e(\gamma_1 + \gamma_2)^{-1}$	0.0348
ϵ_r	Dielectric constant	14.6

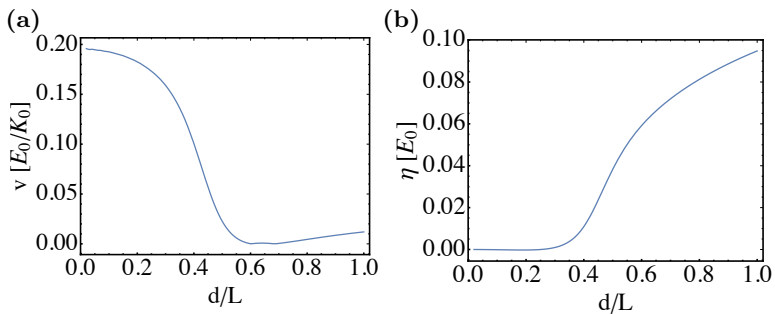


FIG. 2: Parameters of the effective Dirac Hamiltonian (4). (a) Dirac velocity v , in units of E_0/K_0 . (b) spin-orbit gap η , in units of E_0 .

165 The separation along the z -axis of the superlattice top gate from
 166 the 2DHG is z_0 . Although z_0 plays a role [49], we will fix its value
 167 and not consider it further. Moreover, we employ a minimal three
 168 K -point grid for numerical diagonalisation of $H_{2DHG} + W(\mathbf{r})$, which
 169 is used to estimate the couplings entering the effective Dirac Hamil-
 170 tonian (4). In this scheme, W_0 scales out, and so will not explicitly
 171 appear as a free parameter in our analysis. The shortcomings of this
 172 approximation are discussed further in Section VC in relation to the
 173 phase diagram.

174 B. Effective Dirac Hamiltonian

175 Since the periodic potential $W(\mathbf{r})$ has the same symmetries as
 176 the atomic potential in graphene, the bandstructure of the hole gas
 177 with superlattice, i.e. $H_{2DHG} + W(\mathbf{r})$, features Dirac cones at the
 178 high symmetry points \mathbf{K}_i . Performing this diagonalisation explicitly
 179 (see Appendix A), and expanding the resulting Hamiltonian about
 180 the Dirac points, we arrive at the effective Dirac Hamiltonian with
 181 Kane-Mele mass term [54]

$$H_0 = \sum_{\mathbf{p}} \psi_{\mathbf{p}}^\dagger (v(\boldsymbol{\sigma} \cdot \mathbf{p})\tau_z - \mu + \eta\sigma_z s_z) \psi_{\mathbf{p}}. \quad (4)$$

182 the Pauli matrices σ_i , τ_i and s_i act on sub-lattice, valley, and the
 183 effective spin-1/2, and a chemical potential μ describes doping be-
 184 yond the Dirac points. For $\tau = 1$, pseudospin up (down) corresponds
 185 to sublattice A (B), while at the opposite valley $\tau = -1$, pseudospin
 186 up (down) corresponds to sublattice B (A). One may perform a uni-
 187 tary transformation so that the pseudospin has the same definition
 188 at $\tau = -1$ as it does at $\tau = 1$, but intermediate calculations are
 189 made more simple in the basis of (4). At the end of Section IV, we

TABLE II: Transformation properties of operators σ_i , τ_i and s_i under the symmetries of the system: $2\pi/3$ and π rotations C_{3z} , C_{2z} , C_{2x} (for completeness we include C_{2y}), and time reversal \mathcal{T} .

	C_{3z}	C_{2z}	C_{2x}	C_{2y}	\mathcal{T}
s_z	s_z	s_z	$-s_z$	$-s_z$	$-s_z$
σ_z	σ_z	σ_z	$-\sigma_z$	$-\sigma_z$	$-\sigma_z$
τ_z	τ_z	$-\tau_z$	τ_z	$-\tau_z$	$-\tau_z$
τ_{\pm}	τ_{\pm}	τ_{\mp}	τ_{\pm}	τ_{\mp}	τ_{\mp}
σ_{\pm}	$e^{2i\theta_{\pm}}\sigma_{\pm}$	σ_{\pm}	σ_{\mp}	σ_{\mp}	σ_{\mp}

190 shall change to the alternative basis as it makes aspects of our final
 191 results clearer.

192 The symmetries of the system are $2\pi/3$ and π rotations, and time
 193 reversal. The resulting transformation properties of the operators
 194 σ_i , τ_i and s_i are given in Table II.

195 The time-reversal invariant mass term $\eta\sigma_z s_z$ arises from the spin-
 196 orbit interaction and is absent in n -type artificial lattices. This term
 197 gives rise to a \mathbb{Z}_2 topological insulating state. In the Appendix we
 198 show that, in an effective tight-binding description of the artificial
 199 lattice, this term arises due to a spin-dependent complex next near-
 200 est neighbor hopping which is equivalent to two copies of the Hal-
 201 dane model. While the effective Dirac theory is identical to that of
 202 the Kane-Mele model, the hopping phases in the real space descrip-
 203 tion are different, due to the fact that the mass term arises from a
 204 spin-orbit interaction quadratic in momentum, rather than a linear
 205 Rashba spin-orbit interaction.

206 Performing exact diagonalisation of the Luttinger Hamiltonian
 207 (1), with parameters for an InAs 2DHG, we numerically obtain the
 208 Dirac Hamiltonian (4). We plot the Dirac velocity v and spin-orbit
 209 mass gap η as a function of d/L in Fig. 2, in terms of the scale
 210 $E_0 = K_0^2/(2m_H)$, with $K_0 = |\mathbf{K}_i|$. There we see that the effective
 211 Dirac velocity v and the spin-orbit mass gap η depend strongly on
 212 the ratio d/L . The Dirac velocity can be significantly reduced by in-
 213 creasing d/L , flattening the Dirac bands and enhancing interaction
 214 effects.

215 Holes have larger effective masses m_H and moreover, the dis-
 216 persion is non-parabolic – becoming flatter due to an anticrossing
 217 between heavy hole and light hole states (see Appendix A). Band
 218 folding this anticrossing to the Dirac point generates flatter Dirac
 219 bands [53], and correspondingly more localised orbitals; this is con-
 220 trolled by ratio d/L . Such a handle is not available in the analogous
 221 electron-based superlattice honeycomb systems [30, 48].

III. COULOMB MATRIX ELEMENTS

In this section, we will discuss the form of the Coulomb interaction in the effective Dirac theory. By writing the Coulomb interaction in the basis of states near the K and K' points, we find that the Coulomb repulsion contains a short range Hubbard part, which depends on the pseudospin σ , valley τ and effective spin s , extend-

ing earlier results on these models by including spin [1, 30]. The form of these Hubbard interactions are constrained by the symmetry transformations of Table II. Here we directly compute numerically compute the values of the symmetry-allowed matrix elements.

Using the wavefunctions, $|\mathbf{k}, s, \sigma, \tau\rangle$, obtained from diagonalisation of the InAs 2DHG subject to superlattice potential $W(\mathbf{r})$ (3), i.e. $H_{2DHG} + W(\mathbf{r})$, and expanding near the Dirac points, we explicitly compute the matrix elements of the Coulomb interaction,

$$\begin{aligned} \hat{V} &= \langle \mathbf{k}_1, s_4, \sigma_4, \tau_4 | \otimes \langle \mathbf{k}_3, s_3, \sigma_3, \tau_3 | \frac{e^2}{2\epsilon_r |\mathbf{r} - \mathbf{r}'|} | \mathbf{k}_2, s_2, \sigma_2, \tau_2 \rangle \otimes | \mathbf{k}_1, s_1, \sigma_1, \tau_1 \rangle \equiv \frac{2\pi e^2}{\epsilon_r q} + \hat{V}_I + \hat{V}_{II}, \\ \hat{V}_I &= (v_{00}\sigma_0 \otimes \sigma_0 + v_{44}\tau_z s_z \otimes \tau_z s_z) + (v_{33}\tau_z \otimes \tau_z + v_{77} s_z \otimes s_z) \sigma_z \otimes \sigma_z + (v_{12} + v_{56}\tau_z s_z \otimes \tau_z s_z) (\sigma_+ \otimes \sigma_- + \sigma_- \otimes \sigma_+) \\ &\quad + v_{07}(\sigma_0 \otimes \sigma_z s_z + \sigma_z s_z \otimes \sigma_0) + v_{47}(\tau_z s_z \otimes \sigma_z s_z + \sigma_z s_z \otimes \tau_z s_z), \\ \hat{V}_{II} &= \left[u_{00}\sigma_0 \otimes \sigma_0 + u_{33}s_z \otimes s_z + u_{12} (\sigma_+ \otimes \sigma_- + \sigma_- \otimes \sigma_+) + u_{03}(\sigma_0 \otimes \sigma_z s_z + \sigma_z s_z \otimes \sigma_0) \right] (\tau_+ \otimes \tau_- + \tau_- \otimes \tau_+), \end{aligned} \quad (5)$$

Here $\mathbf{q} = \mathbf{k}_1 - \mathbf{k}_3$, and subscripts I and II denote intravalley (τ -diagonal) and intervalley (τ -off-diagonal) interactions. The vertices appearing in the bare interactions are $J_I^\mu \in \{\mathbb{1}, \sigma_\pm, \tau_z \sigma_z, \tau_z s_z, \tau_z s_z \sigma_\pm, \sigma_z s_z\}$, $J_{II}^\mu \in \{\mathbb{1}, \sigma_\pm, \sigma_z s_z\} \otimes \tau_\pm$, which defines the adjoint basis. Using these vertices, the interactions are parametrized $\hat{V}_I^0 = v_{\mu\nu} J_I^\mu \otimes J_I^\nu$ and $\hat{V}_{II}^0 = u_{\mu\nu} J_{II}^\mu \otimes J_{II}^\nu$, which defines the notation in Eq. (5). In Figure 3 we plot the dependence of the coefficients $\{v_{\mu\nu}, u_{\mu\nu}\}$ on the spin-orbit parameter, d/L .

IV. SCREENING

In this section we discuss how the bare Coulomb interactions (5) are modified by screening. A standard approach for analysing the feedback of many body effects on interactions is the Random Phase Approximation [1, 30, 101–104], which involves resumming the infinite series of bubble diagrams which contribute corrections to the bare Coulomb interaction.

The resulting screened interactions $V_{\mu\nu}^R(p_0, \mathbf{p})$ are given by

$$V_{\mu\nu}^R(p_0, \mathbf{p}) = V_{\mu\nu} + V_{\mu\alpha} \Pi^{\alpha\gamma}(p_0, \mathbf{p}) V_{\gamma\nu}^R(p_0, \mathbf{p}) \quad (6)$$

where $\Pi^{\alpha\gamma}$ is the particle-hole polarisation operator, given by

$$\begin{aligned} i\Pi^{\alpha\gamma}(p_0, \mathbf{p}) &= \text{Tr} \int J^\alpha G(q_0 + p_0, \mathbf{q} + \mathbf{p}) J^\gamma G(q_0, \mathbf{q}) \frac{dq_0 d^2\mathbf{q}}{(2\pi)^3}, \\ G(q_0, \mathbf{q}) &= \frac{1}{q_0 + \mu - v\tau_z \mathbf{q} \cdot \boldsymbol{\sigma} - \eta\sigma_z s_z + i0\text{sgn}(q_0)} \quad (7) \end{aligned}$$

where $G(q_0, \mathbf{q})$ is the single particle Green's function. In general, the vertices J^μ, J^ν can be any matrix $\sigma^i \tau^j s^k$ which appears in the bare interactions of the form $V_{\mu\nu} J^\mu \otimes J^\nu$. In this paper we will restrict our attention to the case of static screening, so we neglect the frequency dependence of the polarisation operator and set $p_0 = 0$.

As shown in Section III, the vertices appearing in the bare interactions (5) are $J_I^\mu \in \{\mathbb{1}, \sigma_\pm, \tau_z \sigma_z, \tau_z s_z, \tau_z s_z \sigma_\pm, \sigma_z s_z\}$, $J_{II}^\mu \in \{\mathbb{1}, \sigma_\pm, \sigma_z s_z\} \otimes \tau_\pm$, which defines the adjoint basis. In this basis, the tensor form of the static polarisation operator becomes,

$$\begin{aligned} \hat{\Pi}_I(p_0 = 0, \mathbf{p}) &= \Pi^{\mu\nu}(0, \mathbf{p}) J_I^\mu J_I^\nu, \\ \hat{\Pi}_{II}(p_0 = 0, \mathbf{p}) &= \Pi^{\mu\nu}(0, \mathbf{p}) J_{II}^\mu J_{II}^\nu. \end{aligned} \quad (8)$$

The quantities $\Pi^{\mu\nu}(0, \mathbf{p})$ are evaluated in the Appendix B. We find that only three independent polarisation operators emerge. To gain some insight into their physical meaning, we shall discuss their behavior in the long wavelength limit, $q \rightarrow 0$. First, we find a term $\Pi_0 \rightarrow -\mu N/(2\pi)$, this term corresponds to the usual density-density (Thomas-Fermi) screening, i.e. the vertices coupling to a negative polarisation operator are weakened by screening. Second, $\Pi_z \rightarrow \mu N/(2\pi)$, which corresponds to a pseudospin dipole-dipole *antiscreening*, first discussed in [30] – the positive sign here causes an enhancement of the couplings $v_{33}(\tau_z \sigma_z \otimes \tau_z s_z)$ and $v_{77}(s_z \sigma_z \otimes s_z s_z)$, i.e. those proportional to $\sigma_z \otimes \sigma_z$, which as we shall later see promotes an intravalley $p + i\tau p$ higher topological superconductivity. Similarly, an antiscreening occurs for intervalley terms

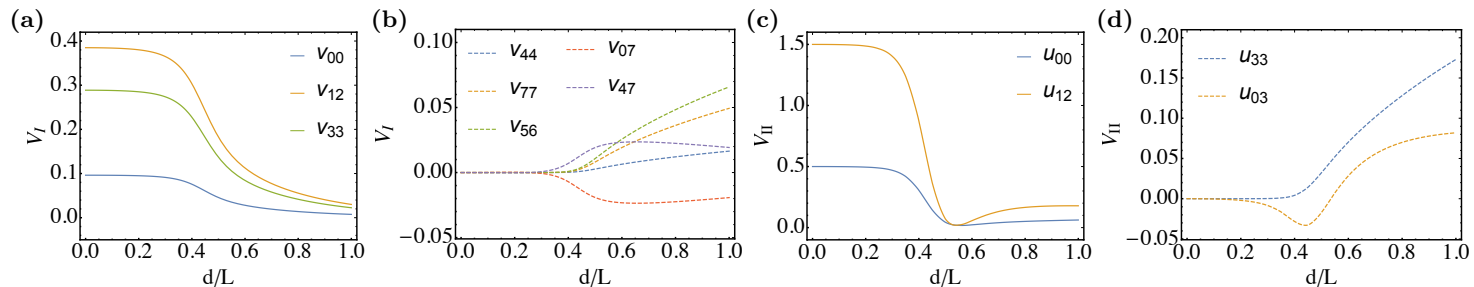


FIG. 3: (a) Spin-independent matrix elements of V_I . Solid lines: blue, orange, green = v_{00}, v_{33}, v_{12} . (b) Spin-dependent matrix elements of V_I . Dashed lines: blue, orange, green, red and purple = $v_{44}, v_{77}, v_{56}, v_{07}, v_{47}$. (c) Spin-independent matrix elements of V_{II} . Solid lines: Blue, green = u_{00}, u_{12} . (d) Spin-dependent matrix elements of V_{II} . Dashed lines: orange, red = u_{33}, u_{03} . In units of $2\pi e^2/(\epsilon_r K_0)$

275 $u_{00}\sigma_0\tau_{\pm}\otimes\sigma_0\tau_{\mp}, u_{33}s_z\tau_{\pm}\otimes s_z\tau_{\mp}$, which acts to favour the higher topo- 296
 276 logical intervalley s_{τ} state. We shall elaborate on this phenomenon
 277 in the following subsection. Third, we have $\Pi_{\eta} \Rightarrow \eta N/(2\pi)$, a di-
 278 rect result of the spin-orbit coupling. Last, we have $\Pi_{\pm} \propto e^{i\theta_{\mathbf{p}}}$, this
 279 Hall-like response, with momentum dependence, promotes interac-
 280 tion matrix elements that were otherwise not present in the bare
 281 interaction structure (5).

282 Inverting the matrix equation (6) is now straightforward and gives,

$$\hat{V}_I^R = v_{\mu\nu}^R J_I^{\mu} J_I^{\nu}, \quad \hat{V}_{II}^R = u_{\mu\nu}^R J_{II}^{\mu} J_{II}^{\nu},$$

283 with superscript R to denote the RPA renormalised values. De-
 284 spite there being a closed form analytic expression, we do not pro-
 285 vide the full expressions for matrix elements $v_{\mu\nu}, u_{\mu\nu}$ since they are
 286 lengthy and unenlightening. The expression (10) defines the RPA-
 287 renormalised interaction structure which we use to search for super-
 288 conducting and magnetic instabilities.

289 Up until this point we have worked in a particular basis for the
 290 single particle Hamiltonian (4), which allowed for straightforward
 291 evaluation of the polarisation operators. However, from this point on
 292 we work in a more physical basis, which will make our later discussion
 293 of the superconducting gap structure more transparent. Performing
 294 a unitary transformation, with $P = \frac{1}{2}(\tau_0 + \tau_z) + \frac{1}{2}(\tau_0 - \tau_z)\sigma_x$, we
 295 obtain

$$\tilde{H}_0 = PH_0P^{\dagger} = vp_x\sigma_x\tau_z + vp_y\sigma_y + \eta s_z\sigma_z\tau_z. \quad (9)$$

The interactions transform as

$$\begin{aligned} \hat{V}_I^R &= v_{\mu\nu}^R (PJ_I^{\mu}P^{\dagger})(PJ_I^{\nu}P^{\dagger}), \\ \hat{V}_{II}^R &= u_{\mu\nu}^R (PJ_{II}^{\mu}P^{\dagger})(PJ_{II}^{\nu}P^{\dagger}), \\ PJ_I^{\mu}P^{\dagger} &\in P\{\mathbb{1}, \tau_z s_z, \tau_z \sigma_z, \sigma_z s_z, \sigma_{\pm}, \tau_z s_z \sigma_{\pm}\}P^{\dagger} \\ &= \{\mathbb{1}, \tau_z s_z, \sigma_z, \tau_z \sigma_z s_z, \sigma_{\pm}^{\tau}, \tau_z s_z \sigma_{\pm}^{\tau}\}, \\ PJ_{II}^{\mu}P^{\dagger} &\in P\{\mathbb{1}, \sigma_z s_z, \sigma_{+}, \sigma_{-}\} \otimes \tau_{\pm} P^{\dagger} \\ &= \{\sigma_x, \pm i\sigma_y s_z, (\sigma_0 \pm \sigma_z)/2, (\sigma_0 \mp \sigma_z)/2\} \otimes \tau_{\pm}. \end{aligned} \quad (10)$$

297 Here $\sigma_{\pm}^{\tau} \equiv \sigma_x \pm i\tau_z \sigma_y$, and in $PJ_{II}^{\mu}P^{\dagger}$, the \pm indices in pseudospin
 298 and valley are connected.

V. SUPERCONDUCTING INSTABILITIES

299
 300 In this section we analyse superconductivity resulting from the
 301 renormalised pseudospin dependent couplings. At a finite doping
 302 away from the Dirac point, the states at the Fermi surface are not
 303 pseudospin eigenstates, but band eigenstates. The interactions (10)
 304 are therefore be rewritten in the basis of band indices, and further-
 305 more since we are only interested in Fermi surface instabilities, we
 306 project onto the upper band (i.e. only include states at the Fermi
 307 surface). The BCS gap equation is then used to calculate T_c for
 308 pairing between these states.

A. Interactions in the Cooper channel

310 To find the superconducting instability, we are interested only in
 311 states near the Fermi surface, which participate in pairing. Hence,
 312 we keep only states in the upper band of (9), the eigenstates of which

are given by

$$|\mathbf{k}, \tau\rangle = \frac{1}{\sqrt{2}} e^{i\mathbf{k}\cdot\boldsymbol{\tau}} (w_{\tau,s}^a(k)|a\rangle + w_{\tau,s}^b(k)e^{i\tau\theta_{\mathbf{k}}}|b\rangle), \quad (11)$$

where $|a\rangle, |b\rangle$ are the σ^z eigenstates, which are localised on the A and B sites respectively, and the wavefunction components, $w_{\tau,s}^a(k) = vk/\sqrt{2\epsilon_k(\epsilon_k - s\tau\eta)}$, $w_{\tau,s}^b(k) = (\epsilon_k - s\tau\eta)w_{\tau,s}^a(k)/(\tau vk)$. To obtain the interactions between Cooper pairs, we perform the following process: (i) project the RPA interaction tensor onto the upper band using (11), (ii) impose the scattering conditions of the Cooper channel $\mathbf{k}_1 = -\mathbf{k}_3$, $\mathbf{k}_2 = -\mathbf{k}_4$, i.e. $\theta_{k_3} = \pi + \theta_{k_1}$, $\theta_{k_4} = \pi + \theta_{k_2}$, (iii) restrict all momenta to lie on the Fermi surface $|\mathbf{k}_i| = k_F$. The interactions then only have angular dependence, and we decompose the resulting Cooper interaction into partial waves with different angular momentum. The result is the coupling between Cooper pairs with a given angular momentum.

Performing such a procedure, we arrive at the couplings in angular momentum channels $\ell = 0, \pm 1$ (higher-order channels are negligible or zero),

$$\hat{V}_{\ell=0} = \tilde{g}_0 + \tilde{g}_1\tau_z \otimes \tau_z + \tilde{g}_2s_z \otimes s_z + \tilde{g}_3s_z\tau_z \otimes s_z\tau_z + (\tilde{j}_0 + \tilde{j}_1s_z \otimes s_z)(\tau_x \otimes \tau_x + \tau_y \otimes \tau_y) \quad (12)$$

$$\hat{V}_{\ell=\pm 1} = g_0 + g_1\tau_z \otimes \tau_z + g_2s_z \otimes s_z + g_3s_z\tau_z \otimes s_z\tau_z + \ell(g_4 + g_5s_zs_z)(\tau_0\tau_z + \tau_z\tau_0) + (j_0 + j_1s_z \otimes s_z + \ell j_2(s_0 \otimes s_0 + s_z \otimes s_0))(\tau_x \otimes \tau_x + \tau_y \otimes \tau_y) \quad (13)$$

The coefficients $g_i, j_i, \tilde{g}_i, \tilde{j}_i$ are functions of chemical potential μ due to the screening effects, as well as the well width to lattice spacing ratio d/L , which controls the strength of the spin-orbit dependent couplings. The (un)tilded couplings correspond to the ($\ell = \pm 1$) $\ell = 0$ partial wave channels. They also depend on the microscopic parameters of the 2DHG; we have evaluated these quantities numerically for an InAs 2DHG. The matrix elements g_i denote intravalley scattering processes, while j_i represent intervalley scattering.

B. Gap equation

The mean field Hamiltonian, which accounts for all pairing possibilities, is

$$\mathcal{H}_{MF} = \sum_{\mathbf{k}, s, \tau} \varepsilon_{\mathbf{k}} \tilde{\psi}_{\mathbf{k}s\tau}^\dagger \tilde{\psi}_{\mathbf{k}s\tau} + \frac{1}{2} \sum_{\mathbf{k}, s, \tau, s', \tau'} \tilde{\psi}_{\mathbf{k}s\tau}^\dagger (\Delta_{\mathbf{k}})_{s\tau, s'\tau'} \tilde{\psi}_{-\mathbf{k}s'\tau'}^\dagger + \text{h.c.} + \frac{1}{2} (\Delta_{\mathbf{k}}^\dagger)_{s_1\tau_1, s_3\tau_3} (\mathcal{V}^{-1})_{\mathbf{k}, \mathbf{p}; s_1\tau_1 s_2\tau_2 s_3\tau_3 s_4\tau_4} (\Delta_{\mathbf{p}})_{s_4\tau_4, s_2\tau_2} \quad (14)$$

where $\tilde{\psi}_{\mathbf{k}s\tau}^\dagger$ is the hole creation operator for the upper band. We parametrize the gap in the standard form, collecting the spin, valley and angular momentum structure into a tensor $d_\ell^{\mu\nu}$,

$$\Delta_{\mathbf{k}} = \sum_{\mu\nu, l} d_\ell^{\mu\nu} s_\mu \tau_\nu e^{-il\theta_{\mathbf{k}}} (\tau_y s_y) \quad (15)$$

The spin and valley structure follows from the usual singlet-triplet decomposition (dropping the angular momentum index ℓ) [105],

$$\begin{aligned} d^{\mu\nu} &= d_s^\mu \otimes d_v^\nu, \\ d_s^x &= \frac{1}{2} (|\uparrow\uparrow\rangle - |\downarrow\downarrow\rangle) & d_s^y &= \frac{1}{2i} (|\uparrow\uparrow\rangle + |\downarrow\downarrow\rangle) \\ d_s^z &= -\frac{1}{2} (|\uparrow\downarrow\rangle + |\downarrow\uparrow\rangle) & d_s^0 &= \frac{1}{2} (|\uparrow\downarrow\rangle - |\downarrow\uparrow\rangle), \\ d_v^x &= \frac{1}{2} (|++\rangle - |--\rangle) & d_v^y &= \frac{1}{2i} (|++\rangle + |--\rangle) \\ d_v^z &= -\frac{1}{2} (|+-\rangle + |-+\rangle) & d_v^0 &= \frac{1}{2} (|+-\rangle - |-+\rangle). \end{aligned}$$

where subscript s indicates spin and v indicates valley. The BCS gap equation is given by

$$\begin{aligned} d_\ell^{\mu\nu} &= -G_{\mu\nu; \delta\gamma}^\ell \int_0^{\varepsilon_c} \frac{Nd\varepsilon}{2\pi v^2} \frac{\varepsilon}{2E(d_\ell^{\delta\gamma})} \tanh\left(\frac{E(d_\ell^{\delta\gamma})}{2T}\right), \\ E(d_\ell^{\delta\gamma}) &= \sqrt{(\varepsilon - \mu)^2 + |d_\ell^{\delta\gamma}|^2} \end{aligned} \quad (16)$$

where the matrix $G_{\mu\nu; \delta\gamma}$ is given by

$$G_{\mu\nu; \delta\gamma}^\ell \equiv \frac{1}{4} (\hat{s}_\mu \hat{s}_y)_{ac}^\dagger (\hat{\tau}_\nu \hat{\tau}_y)_{a'c'}^\dagger (\hat{V}_\ell)_{abcd; a'b'c'd'} (\hat{s}_\delta \hat{s}_y)_{bd} (\hat{\tau}_\gamma \hat{\tau}_y)_{b'd'} \quad (17)$$

To determine the dominant instability $d^{\mu\nu}$, we find the gap function with highest T_c via the eigenvalue problem (with eigenvalue $\lambda_{\mu\nu}^\ell$)

$$G_{\mu\nu; \delta\gamma}^\ell d_\ell^{\delta\gamma} = \lambda_{\mu\nu}^\ell d_\ell^{\mu\nu}. \quad (18)$$

Substitution of the eigenvectors $d^{\mu\nu}$ into the gap equation then results in

$$\begin{aligned} 1 &= -\nu_0 \lambda_{\mu\nu}^\ell L(T_c, \mu, \varepsilon_c), \\ L(T_c, \mu, \varepsilon_c) &= \int_0^{\varepsilon_c} \frac{d\varepsilon \varepsilon / \mu}{2|\varepsilon - \mu|} \tanh\left(\frac{|\varepsilon - \mu|}{2T_c}\right), \quad \nu_0 = \frac{N\mu}{2\pi v^2}, \end{aligned} \quad (19)$$

where ν_0 is the density of states at the Fermi level, and ε_c is an ultraviolet cut-off. The logarithmic behavior of $L(T_c, \mu, \varepsilon_c)$ gives rise to the exponential dependence of $T_c \sim \varepsilon_c e^{-1/(\nu_0 \lambda_{\mu\nu}^\ell)}$ on the density of states ν_0 and the eigenvalue $\lambda_{\mu\nu}^\ell$, which must be negative for the gap equation to have a solution, corresponding to an attractive interaction.

Using the explicit form of the interactions (12) and (13), we find the three dominant gap structures, with the following (negative) eigenvalues of G (17),

$$d_{\ell=\pm 1}^{x\mp} : \lambda_{x\pm}^{\mp 1} = g_0 + g_1 + g_2 + g_3 - g_4 - g_5, \quad (20a)$$

$$d_{\ell=\pm 1}^{zz} : \lambda_{zz}^{\pm 1} = g_0 - g_1 - g_2 + g_3 + j_0 + j_1, \quad (20b)$$

$$d_{\ell=0}^{z0} : \lambda_{z0}^0 = \tilde{g}_0 - \tilde{g}_1 - \tilde{g}_2 + \tilde{g}_2 - \tilde{j}_0 - \tilde{j}_1. \quad (20c)$$

These gap structures will be described in detail in Section V C.

We pause to discuss the mechanism of attraction explicitly in reference to these eigenvalues (20a)-(20c). We focus on terms that do not contain s_z in (12) and (13), since these drive the transition, while s_z dependent terms act to fix the spin orientation of the corresponding spin-triplet states.

For $\ell = 0$, we identify the driving term for superconductivity as $\tilde{j}_0(\tau^x \otimes \tau^x + \tau^y \otimes \tau^y)$, whereas for $\ell = \pm 1$, the driving term for superconductivity is $g_0(\tau_0 \otimes \tau_0)$. The coupling \tilde{j}_0 is positive, and antiscreening increases its magnitude as the chemical potential increases. Hence choosing a valley singlet structure generates a negative eigenvalue $-\tilde{j}_0$, analogous to how antiferromagnetism promotes spin singlet pairing. Antiscreening in g_0 manifests as a sign change – for large enough chemical potential, g_0 is overscreened and becomes negative, as has been previously discussed in Refs [1, 30].

C. Explicit solution and phase diagram

In this section we construct the phase diagram consisting of the three leading superconducting instabilities of (20a)-(20c), as well as for competing charge and magnetic order, which will be described in Section VI.

We specify the phase diagram as follows: (a) we choose to fix the ratio $d/L = 0.375$, which as we have stated earlier quantifies the strength of spin-orbit coupling, with a physically achievable $L = 30$ nm. Other (similar) values of d/L will act to affect the phase boundaries, but not the phases themselves. (b) We designate a *critical doping* $\mu_c = 0.025vK_0$ and plot phase diagrams for $\mu/\mu_c = \{0.75, 1, 1, 25\}$. (c) We use the magnitude of the bare interaction matrix elements, $u_{\mu\nu}, v_{\mu\nu}$ – i.e. $v_{12}, v_{33}, u_{00}, u_{12}$ from (5) – as continuous tuning parameters. As shown in Fig. 4, we plot two sets of diagrams spanned by $(\tilde{v}_{12}/v_{12}, \tilde{u}_{12}/u_{12})$ and $(\tilde{v}_{33}/v_{33}, \tilde{u}_{00}/u_{00})$.

The motivation for choice (c) is that one expects quantitative changes to the values of bare interaction matrix elements (5), shown in Fig. 3, for four reasons: (i) inaccuracies of the microscopic modeling, such as those due to neglecting higher harmonics in (3), i.e.

additional cosine terms which respect the honeycomb symmetry, as discussed in [49]; (ii) corrections to the infinite square well potential (2); (iii) corrections of order W_0/E_0 , which are not captured in the three K -point approach; finally (iv) since we only present results for an InAs heterostructure, the variation in the calculated bare values may be very approximately linked to teasing out the phase diagram for other choices of semiconductor heterostructures. Hence, instead of incorporating all such corrections numerically, we will allow the bare interaction parameters to vary about the values presented in Fig. 3. In this way we absorb uncertainty due to microscopic details of the superlattice potential into the numerical values of the bare interaction parameters v_{ij}, u_{ij} (5).

The dominant bare interactions are found to be $v_{12}, v_{33}, u_{00}, u_{12}$, as shown in Figure 3, and for the purposes of presentation, we choose to vary these four parameters. Denoting the freely varying parameters as $\tilde{v}_{12}, \tilde{v}_{33}, \tilde{u}_{00}, \tilde{u}_{12}$, in Figure 4, we plot two sets of spanned by $(\tilde{v}_{12}/v_{12}, \tilde{u}_{12}/u_{12})$ and $(\tilde{v}_{33}/v_{33}, \tilde{u}_{00}/u_{00})$.

As anticipated in (20a),(20b),(20c), three distinct gap structures appear in the phase diagram, which we describe here:

- **Intravalley $p + i\tau p$ spin-triplet, valley-triplet,**

$$\Delta_{\mathbf{k}} = e^{i\tau_z(\phi - \theta_{\mathbf{k}})}(d_s^x s_x + d_s^y s_y)\tau_y (\tau_y s_y) \quad (21)$$

The spin triplet vector is pinned in-plane, and the valley polarization is coupled to the orbital angular momentum, i.e. $\ell = \pm 1$ at valley $\tau = \mp 1$. This implies a chiral p -wave gap, with opposite chiralities in each valley, a state which respects time reversal symmetry. This phase exhibits a $U(1) \times U(1)$ symmetry breaking due to the presence of a relative phase ϕ between opposite valleys and a spin direction $\mathbf{d}_s = (d_s^x, d_s^y, 0)$. The superconducting state is analogous to that of Ref. [30] but with \mathbf{d} pinned in-plane. This state exhibits higher-order topology, as will be demonstrated in Section VII.

- **Intervalley $p + ip$ spin-triplet, valley-triplet,**

$$\Delta_{\mathbf{k}} = e^{\pm i\theta_{\mathbf{k}}} d_s^z s_z \tau_z (\tau_y s_y) \quad (22)$$

Here the chiral angular momentum states $\ell = \pm 1$ are degenerate. An analysis of the Landau-Ginzburg free energy is required to understand if these degenerate states compete or co-exist. A simple computation gives the Landau-Ginzburg free energy for the two order parameters $e^{\pm i\theta_{\mathbf{k}}} s_z \tau_z \equiv \phi_{\pm}$,

$$\mathcal{F}[\phi_{\pm}] = -s(\phi_+^2 + \phi_-^2) + \alpha(\phi_+^4 + 4\phi_+^2\phi_-^2 + \phi_-^4) \quad (23)$$

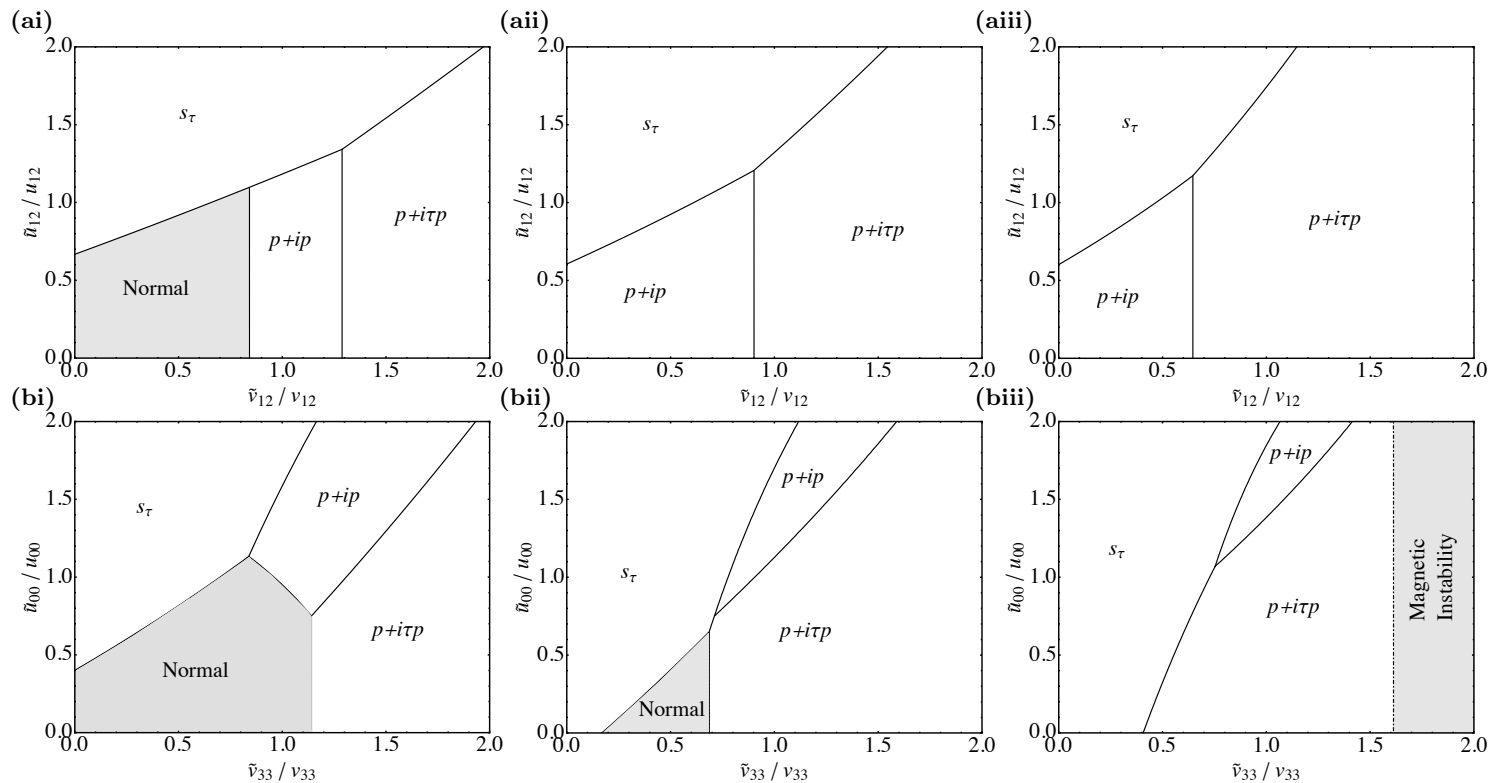


FIG. 4: Phase diagram. The three superconducting phases $d_{z0}^{\ell=0}$, $d_{zz}^{\ell=\pm}$, $d_{\ell=\pm}^{\alpha\pm}$, which correspond to s -wave intervalley (s_τ), $p + ip$ -wave intervalley ($p + ip$), and $p + i\tau p$ intravalley ($p + i\tau p$), as well as the magnetic phase. (a) Fixing the bare values $\{v_{00}, v_{33}, v_{44}, v_{77}, v_{56}, v_{07}, v_{47}, u_{00}, u_{33}, u_{03}\}$ to those computed and shown in Figure 3, while allowing for a variable \tilde{v}_{12} and \tilde{u}_{12} , which are substituted into the interaction structure in place of v_{12} and u_{12} . Here we show the variable values as ratio of the calculated values. (ai), (aii), (aiii) Show the same parameters but with increasing chemical potential $\mu/\mu_0 = 0.75, 1, 1.25$, respectively, with $\mu_0 \equiv 0.025vK_0$, with $d/L = 0.375$, $L = 30\text{nm}$. (b) Same as (a), but allowing for a variable \tilde{v}_{33} and \tilde{u}_{00} . (bi), (bii), (biii) Show the same parameters but with increasing chemical potential $\mu/\mu_0 = 0.75, 1, 1.25$.

432 The quartic term breaks the $SO(2)$ rotational symmetry in 444
 433 the isospin space (ϕ_+, ϕ_-), and the order parameters ϕ_\pm act 445
 434 like an Ising degree of freedom; the system must spontaneously 446
 435 choose a chirality ($\ell = \pm 1$), and therefore spontaneously break 447
 436 time reversal symmetry. This phase possesses a nontrivial first- 448
 437 order topological invariant which manifests as chiral modes 449
 438 propagating along the edge, as we discuss in Section VII. 450

- 439 • **Intervalley s_τ** spin-triplet, valley-singlet,

$$\Delta_{\mathbf{k}} = d_s^z s_z \tau_0 (\tau_y s_y) \quad (24)$$

440 The spin triplet vector is pinned out-of-plane along z . As 455
 441 shown in [106], owing to the valley singlet structure, this spin 456
 442 triplet phase satisfies an “Anderson theorem”, which provides 457
 443 protection against non-magnetic disorder, provided the disorder 458

444 does not induce intervalley scattering. Quite unexpectedly, 445
 446 this phase hosts a second-order topological invariant, to 447
 448 be described in Section VII. 449

450 As can be seen in Figure 4, for each superconducting state there is 451
 452 a critical μ_c such that for $\mu > \mu_c$ the system becomes superconducting, 453
 454 which as discussed earlier reflects the fact that as the chemical 455
 456 potential is increased, screening becomes more efficient, causing the 457
 458 pseudospin and/or valley dependent interactions to become attractive. 459

459 Note that the phase boundaries between normal and superconducting 460
 461 states are second-order, while the phase boundaries between 462
 463 distinct superconducting states are first-order, which in principle 464
 465 leaves open the possibility of coexistence between these superconducting 466
 467 phases. However, a straightforward Landau-Ginsburg analysis shows that all 468
 469 coexistence is energetically penalised. 470

459 Finally, the rightmost portion of Figure 4 contains a region la-
 460 belled as a “magnetic instability”. In this region, we find that mag-
 461 netic insulating states can compete with superconductivity, as we
 462 will discuss in Section VI.

463 VI. COMPETING INSTABILITIES

464 In this section we address the question of whether other instabili-
 465 ties may compete with superconductivity. As is expected in general,
 466 superconductivity dominates in the limit of weak interactions when
 467 the Fermi surface is not nested. We find a portion of the phase di-
 468 agram at stronger couplings in which magnetic order dominates, as
 469 shown in Figure 4.

470 We consider three types of instabilities: ferromagnetism (FM),
 471 spin density wave (SDW), and charge density wave (CDW), where
 472 the SDW and CDW states are commensurate with the lattice with
 473 period \mathbf{K} . These phases are referred to as particle-hole instabilities,
 474 and are captured by the order parameters, respectively

$$\begin{aligned}\Phi_1 &= \sum_{\mathbf{k}} \psi_{\uparrow,\tau,\mathbf{k}}^\dagger \psi_{\downarrow,\tau,\mathbf{k}}, \\ \Phi_2 &= \sum_{\mathbf{k}} \psi_{\uparrow,\tau,\mathbf{k}}^\dagger \psi_{\downarrow,-\tau,\mathbf{k}}, \\ \Phi_3 &= \sum_{\mathbf{k}} \psi_{\uparrow,\tau,\mathbf{k}}^\dagger \psi_{\uparrow,-\tau,\mathbf{k}}.\end{aligned}\quad (25)$$

475 These orders take hold when their associated susceptibilities

476 diverge, a condition which results in equations analogous to
 477 the BCS gap equation. Denoting the particle-hole susceptibility
 478 $\chi_{s_1\tau_1,s_2\tau_2}(p_0, \mathbf{p})$, FM order corresponds to a divergence in $\chi_1 =$
 479 $\chi_{s\tau,-s\tau}(0, \mathbf{0})$, SDW order to $\chi_2 = \chi_{s\tau,-s-\tau}(0, \mathbf{0})$ and CDW to
 480 $\chi_3 = \chi_{s\tau,s-\tau}(0, \mathbf{0})$.

481 In the previous section, we wrote the interactions in the basis of
 482 states in the upper band (ie at the Fermi surface) with $\mathbf{k}_1 = -\mathbf{k}_3$,
 483 $\mathbf{k}_2 = -\mathbf{k}_4$, corresponding to the Cooper scattering channel. For the
 484 particle-hole instabilities, the relevant scattering amplitudes are the
 485 direct and exchange channels. We again restrict all momenta to lie
 486 on the Fermi surface $|\mathbf{k}_i| = k_F$. The scattering condition for the
 487 exchange channel is $\mathbf{k}_1 = \mathbf{k}_4$, $\mathbf{k}_2 = \mathbf{k}_3$, with scattering angle $\theta \equiv$
 488 $\theta_{k_2} - \theta_{k_1}$. The corresponding couplings \mathcal{V} are obtained analogously
 489 to the procedure in the Cooper channel (C3). We further define the
 490 $\ell = 0$ component as $\int d\theta \hat{V}/(2\pi) \equiv \hat{\mathcal{V}}^X$. For the density channel,
 491 $\mathbf{k}_1 = \mathbf{k}_2$, $\mathbf{k}_3 = \mathbf{k}_4$, with scattering angle $\theta \equiv \theta_{k_3} - \theta_{k_1}$, and we define
 492 the $\ell = 0$ component as $\int d\theta \hat{V}/(2\pi) \equiv \hat{\mathcal{V}}^D$. The procedure of the
 493 previous section yields the tensor,

$$\begin{aligned}\hat{\mathcal{V}}^X &= g_0^X + g_1^X \tau_z \otimes \tau_z + g_2^X s_z \otimes s_z + g_3^X s_z \tau_z \otimes s_z \tau_z \\ &\quad + (j_0^X + j_1^X s_z \otimes s_z) (\tau_+ \otimes \tau_- + \tau_- \otimes \tau_+) \\ \hat{\mathcal{V}}^D &= j_0^D (\tau_+ \otimes \tau_- + \tau_- \otimes \tau_+)\end{aligned}\quad (26)$$

494 The ladder equations give the total susceptibilities in terms of the
 495 static susceptibilities and the direct/exchange scattering amplitudes,

$$\begin{aligned}\chi_{s_1\tau_1,s_2\tau_2}(0, \mathbf{0}) &= \chi_{s_1\tau_1,s_2\tau_2}^0(0, \mathbf{0}) + \sum_{s_a,s_b,\tau_a,\tau_b} \int \frac{d^3q_1 d^3q_2}{(2\pi)^6} G_{s_1\tau_1}(q_{10}, \mathbf{q}_1) G_{s_2\tau_2}(q_{10}, \mathbf{q}_1) V_{s_1\tau_1 s_a \tau_a, s_2\tau_2 s_b \tau_b}(\theta_2 - \theta_1) G_{s_a\tau_b}(q_{20}, \mathbf{q}_2) G_{s_b\tau_b}(q_{20}, \mathbf{q}_2) + \dots \\ &= \chi_{s_1\tau_1,s_2\tau_2}^0(0, \mathbf{0}) + \chi_{s_1\tau_1,s_2\tau_2}^0(0, \mathbf{0}) \sum_{s_a,s_b,\tau_a,\tau_b} \left(\int \frac{d\theta}{2\pi} V_{s_1\tau_1 s_a \tau_a, s_2\tau_2 s_b \tau_b}(\theta_2 - \theta_1) \right) \chi_{s_a\tau_a, s_b\tau_b}(0, \mathbf{0}) \\ &= \chi_{s_1\tau_1,s_2\tau_2}^0(0, \mathbf{0}) + \chi_{s_1\tau_1,s_2\tau_2}^0(0, \mathbf{0}) \sum_{s_a,s_b,\tau_a,\tau_b} \mathcal{V}_{s_1\tau_1 s_a \tau_a, s_2\tau_2 s_b \tau_b}^{X/D} \chi_{s_a\tau_a, s_b\tau_b}(0, \mathbf{0}).\end{aligned}$$

496 where the static susceptibilities are given by

$$\chi_{s_1\tau_1,s_2\tau_2}^0(0, \mathbf{0}) \equiv -i \int \frac{d^3q}{(2\pi)^3} G_{s_1\tau_1}(q_0, \mathbf{q}) G_{s_2\tau_2}(q_0, \mathbf{q}). \quad (27)$$

497 For FM, SDW, and CDW order, we evaluate the relevant static
 498 susceptibilities as $\chi_{s\tau,-s\tau}^0(q_0 = 0, \mathbf{q} = 0) = \chi_{s\tau,-s-\tau}^0(q_0 = 0, \mathbf{q} =$
 499 $0) = \chi_{s\tau,s-\tau}^0(q_0 = 0, \mathbf{q} = 0) = \mu/(2\pi)$. The resulting RPA equations

500 for the susceptibilities reduce to

$$\begin{aligned}\chi_1 &= \frac{\mu}{2\pi} + \frac{\mu}{2\pi} \left(\hat{\mathcal{V}}_{s+s+, \bar{s}+\bar{s}+}^X + \hat{\mathcal{V}}_{s+s-, \bar{s}-\bar{s}+}^X \right) \chi_1, \\ \chi_2 &= \frac{\mu}{2\pi} + \frac{\mu}{2\pi} \left(\hat{\mathcal{V}}_{s+s+, \bar{s}-\bar{s}-}^X \right) \chi_2, \\ \chi_3 &= \frac{\mu}{2\pi} + \frac{\mu}{2\pi} \left(\hat{\mathcal{V}}_{s+s-, s-s+}^D \right) \chi_3.\end{aligned}\quad (28)$$

501 The condition for FM, SDW and CDW instabilities immediately

502 follow, and can be written analytically in terms of the coupling con-
503 stants found in (26),

$$\begin{aligned}
 \text{(FM): } 1 &= \frac{\mu}{2\pi} \left(\hat{\mathcal{V}}_{s+s+, \bar{s}+\bar{s}+}^X + \hat{\mathcal{V}}_{s+s-, \bar{s}-\bar{s}+}^X \right) \\
 &= \frac{\mu}{2\pi} (g_0^X + g_1^X - g_2^X - g_3^X + j_0^X - j_1^X) \\
 \text{(SDW): } 1 &= \frac{\mu}{2\pi} \hat{\mathcal{V}}_{s+s+, \bar{s}-\bar{s}-}^X = \frac{\mu}{2\pi} (g_0^X - g_1^X - g_2^X + g_3) \\
 \text{(CDW): } 1 &= \frac{\mu}{2\pi} \hat{\mathcal{V}}_{s+s-, s-s+}^D = \frac{\mu}{2\pi} j_0^D. \tag{29}
 \end{aligned}$$

504 From Eq. (29), the system exhibits instabilities which compete
505 with superconductivity when the dimensionless coupling constants
506 are order unity – as distinct from the superconducting instability
507 which occurs for arbitrarily weak attractive coupling. Throughout
508 most of the phase diagram we considered, this condition is not met,
509 and so superconductivity is the sole instability of the system.

510 Increasing the chemical potential, the antiscreening mechanism
511 causes the g_0 coupling to grow large. Since this coupling does not
512 appear in the susceptibility for CDW order, antiscreening gives rise
513 to only FM and SDW ordering. We do find one small region of phase
514 diagram where g_0 grows large enough to give rise to FM and SDW
515 order. The other couplings, which are much smaller than g_0 , act to
516 favor SDW over FM order. In the phase diagram we simply label
517 this region as *magnetic instability* since we expect FM and SDW
518 to be nearly degenerate. Moreover, this part of the phase diagram
519 should not be taken too literally, since the large coupling constant
520 means corrections to mean field theory are likely significant.

521 VII. TOPOLOGICAL PROPERTIES OF THE 522 SUPERCONDUCTING PHASES

523 In this section we will prove that all three superconducting phases
524 are topological, and discuss their properties. For intervalley pairing,
525 we have $\Delta_{\mathbf{k}} \propto \tau_y$ and $\Delta_{\mathbf{k}} \propto e^{\pm i\theta_{\mathbf{k}}} \tau_x$ for the s_τ and $p + ip$ phases
526 respectively, while $\Delta_{\mathbf{k}} \propto e^{i\tau_z(\phi - \theta_{\mathbf{k}})}$ for the intravalley $p + i\tau p$ phase.
527 Since $\tau_x, \hat{\tau}_z$ are even under inversion ($\mathbf{r} \rightarrow -\mathbf{r}$) while τ_y is odd, we
528 find that the gap is odd under inversion for both intervalley phases,
529 while the intravalley $p + i\tau p$ phase is even for $\phi = n\pi$ and odd
530 for $\phi = (n + \frac{1}{2})\pi$, with $n \in \mathbb{Z}$. A fundamental requirement for a
531 non trivial topology hosting Majorana edge or corner modes is that
532 the gap change sign under inversion¹. This is fulfilled for both the

533 intervalley phases, as well as for the intravalley $p + i\tau p$ phase in the
534 special case $\phi = (n + \frac{1}{2})\pi$.

535 The time-reversal symmetry breaking intervalley $p + ip$ phase
536 exhibits first-order topology; taking into account the $U(1)$ spin-
537 rotation symmetry, we find that this system is in Cartan class A,
538 which permits a Chern number in two dimensions [107, 108]. We
539 find that this phase exhibits a pair of chiral Dirac modes propagat-
540 ing along the boundary, establishing it as a first-order topological
541 superconductor.

542 The intervalley s_τ phase is time-reversal symmetric, and account-
543 ing for the $U(1)$ spin-rotation symmetry, is in class AIII, which
544 always implies trivial first-order topology in two dimensions. The
545 time-reversal symmetric intravalley $p + i\tau p$ satisfies a \mathbb{Z}_2 symmetry
546 expressed by a combination of spin rotation and gauge transforma-
547 tion, such that the system is described by a BdG Hamiltonian in
548 class D. For intervalley s_τ and intravalley $p + i\tau p$, a second-order
549 topological phase protected by the crystalline symmetries is possible.
550 We will establish the second-order topology for intravalley $p + i\tau p$
551 and intervalley s_τ pairing using symmetry-based indicators. Finally,
552 we will present exact diagonalisation results for the Bogoliubov-de
553 Gennes Hamiltonian for all three superconducting phases. These nu-
554 merical results provide clear evidence for the suggested topology by
555 demonstrating the corresponding anomalous edge and corner states.

556 It is first necessary to express the mean field Hamiltonian (14)
557 as a lattice model involving creation operators $c_{\mathbf{R},s}^\dagger$ for Wannier or-
558 bitals localised at the sites \mathbf{R} of the artificial honeycomb lattice,
559 $\mathcal{H}_{\text{MF}} = \mathcal{H}_{\text{nor.}} + \mathcal{H}_\Delta$. The normal state Hamiltonian $\mathcal{H}_{\text{nor.}}$ is equiva-
560 lent to two copies of the Haldane model, consisting of a sum of spin-
561 independent nearest neighbour hoppings and next nearest neigh-
562 bour spin-dependent hopping terms,

$$\mathcal{H}_{\text{nor.}} = - \sum_{\langle \mathbf{R}, \mathbf{R}' \rangle; s} t c_{\mathbf{R},s}^\dagger c_{\mathbf{R}',s} - \sum_{\langle \langle \mathbf{R}, \mathbf{R}' \rangle \rangle; s} t' e^{\frac{2\pi i}{3} \sigma_s} c_{\mathbf{R},s}^\dagger c_{\mathbf{R}',s} \tag{30}$$

563 where the parameters of the Dirac model (9) are related to the hop-
564 ping parameters via $v = \sqrt{3}at/2$ and $t' = 9\eta/2$.

and the gap is even under inversion, the topological classification with inversion symmetry is trivial. This implies that a first-order topological phase hosting a helical Majorana edge mode, as well as a second-order topological phase hosting Kramers pairs of Majorana corner state, is prohibited. When more symmetries are included it is still possible that further topological phases appear, however they must have distinct boundary signatures from the ones mentioned.

¹ A close examination of the classification presented in Refs. [4, 8] reveals that when the system respects time-reversal symmetry, i.e. in Cartan class DIII,

565 The pairing term H_Δ is given by

$$H_\Delta = \sum_{\mathbf{R}, \mathbf{R}'} \Delta(\mathbf{R}, \mathbf{R}') c_{\mathbf{R}, \uparrow}^\dagger c_{\mathbf{R}, \downarrow}^\dagger \quad (31)$$

566 for the intervalley $p+ip$ and s_τ phases with pairing between opposite
567 spins, and

$$H_\Delta = \sum_{\mathbf{R}, \mathbf{R}'} \Delta(\mathbf{R}, \mathbf{R}') \frac{1}{2} \left[e^{i\phi_s} c_{\mathbf{R}, \uparrow}^\dagger c_{\mathbf{R}', \uparrow}^\dagger + e^{-i\phi_s} c_{\mathbf{R}, \downarrow}^\dagger c_{\mathbf{R}', \downarrow}^\dagger \right] \quad (32)$$

568 for the intravalley $p+i\tau p$ phase with equal spin pairing, where
569 $(d_x, d_y, d_z) = (\sin \phi_s, \cos \phi_s, 0)$. The form of the pairing function
570 $\Delta(\mathbf{R}, \mathbf{R}')$ may be derived by projecting the momentum-space ex-
571 pression for H_Δ in (14) onto the Wannier orbitals, and are derived
572 in the Appendix. For the intervalley paired phases, $\Delta(\mathbf{R}, \mathbf{R}')$ pos-
573 sesses the discrete translational symmetry of the lattice and changes
574 sign under inversion, $\Delta(-\mathbf{R}, -\mathbf{R}') = -\Delta(\mathbf{R}, \mathbf{R}')$, while for the in-
575 travalley $p+i\tau p$ phase, the discrete translation symmetry of the
576 lattice is spontaneously broken and $\Delta(\mathbf{R}, \mathbf{R}')$ exhibits spatial mod-
577 ulations, oscillating as a function of $\mathbf{R} + \mathbf{R}'$ and, except at special
578 values $\phi = n\pi/2$, also spontaneously breaks inversion symmetry.

579 A. Symmetry-based indicators for $p+i\tau p$ and s_τ phases

580 In this subsection, we prove that the superconducting states with
581 $p+i\tau p$ or s_τ pairing symmetry realise a second-order topological
582 phase with Majorana Kramers pairs pinned to the corners by the
583 crystalline point-group symmetries. We will first examine the sym-
584 metries of the system to determine under which conditions we may
585 expect a second-order topological phase. Next, we apply the theo-
586 ry of symmetry-based indicators [5–7] to derive a simple, sufficient
587 criterion for a transition into a second-order topological supercon-
588 ducting state when an infinitesimal pairing which is odd under in-
589 version symmetry creates a full gap in the BdG spectrum. Finally,
590 we show that this criterion is fulfilled for the $p+i\tau p$ and s_τ pairing
591 instabilities in our honeycomb lattice model.

592 The symmetry-group of our hexagonal lattice is given by the di-
593 rect product of translations in the x, y plane and the crystalline point
594 group $D_{6h} \simeq C_{6v} \otimes C_i$, where C_i is generated by spatial inversion
595 $\mathcal{I} : x, y, z \rightarrow -x, -y, -z$ and C_{6v} is the point group of the hexagonal
596 lattice in the x, y plane. Furthermore, the normal-state Hamiltonian
597 satisfies time-reversal symmetry \mathcal{T} and $U(1)$ spin rotation symmetry
598 \mathcal{S} around the s_z axis. A symmetric unit cell can be chosen to co-
599 incide with the hexagons in the hexagonal lattice, where the lattice
600 sites are located on the threefold rotation symmetric corners of the

601 hexagonal unit cell. Each site is occupied by one Kramers pair of
602 fermionic orbitals, which, without loss of generality for the following
603 discussion, can be chosen to be s -orbitals². In the following, we ar-
604 gue that inversion symmetry is sufficient to protect the second-order
605 topological phase and prove its appearance from the symmetry-based
606 indicator. Therefore, it is sufficient to consider the representations
607 of time-reversal symmetry and inversion symmetry. In Bloch basis,
608 these representations in the normal state can be written as

$$\begin{aligned} u(\mathcal{T}) &= i s_y \sigma_0 \\ u(\mathcal{I}; \mathbf{k}) &= s_0 \sigma_x e^{i(\mathbf{a}_2 - \mathbf{a}_1) \cdot \mathbf{k}} \end{aligned} \quad (33)$$

609 with s_i, σ_i the Pauli matrices in spin and sublattice space, re-
610 spectively, and the Bravais lattice vectors $\mathbf{a}_1 = \sqrt{3}a\hat{x}$, $\mathbf{a}_2 =$
611 $(\sqrt{3}a\hat{x} + 3a\hat{y})/2$, where a is the interatomic distance. Here we chose
612 the center of the hexagons as the center of inversion.

613 The $p+i\tau p$ and s_τ superconducting orders preserve time-reversal
614 symmetry. Out of the large symmetry-group containing the point
615 group D_{6h} and \mathbb{Z}_2 or $U(1)$ spin rotation symmetry, respectively, it
616 is sufficient to preserve only a single crystalline symmetry element
617 such as inversion, perpendicular twofold rotation, or mirror symme-
618 try in order to protect a second-order topological phase [4, 8]. Here,
619 we focus on inversion symmetry, as it also allows us to write down a
620 symmetry-based indicator as a topological invariant. By restricting
621 the topological classification to inversion and time-reversal symmetry
622 and neglecting the remaining symmetries, we resolve the topological
623 phases in Cartan class DIII with inversion symmetry³. The remain-
624 ing symmetry elements apart from time-reversal and inversion may
625 enrich these topological phases, either prohibiting or giving rise to
626 further topological phases. For example, the $U(1)$ spin rotation sym-
627 metry prohibits the first-order topological superconductor in Cartan
628 class DIII with helical Majorana edge states. The mirror and sixfold
629 rotation symmetry enrich the second-order topological phase pro-
630 tected by inversion, as the mirror symmetry pins the corner states

² The s -orbitals are even under inversion. Choosing different orbitals may change the representation of inversion symmetry that is carried through the calculation, but does not affect the conclusions.

³ Notice that previously, we took the $U(1)$ spin-rotation symmetry or \mathbb{Z}_2 combined spin-gauge symmetry into account to conclude that each of the spin-blocks is in Cartan class AIII or D, respectively. Here, we only utilize a minimal set of symmetries that is necessary to protect the second-order topological phase whose existence we want to prove, which does not require additional $U(1)$ or \mathbb{Z}_2 symmetry. Thus we may utilize the results for the less restrictive class DIII.

to mirror-symmetric corners and at the same time requires a gapless anomalous edge state on mirror symmetric edges [3, 4], while the sixfold rotation symmetry requires that on a sixfold symmetric sample, gapless states should exist on all six corners.

The topological classification depends on whether the superconducting order parameter is even or odd under inversion; this parity determines the representation of inversion symmetry and its commutation relations with the particle-hole antisymmetry of the BdG Hamiltonian [5, 7]. In case the superconducting order parameter is even under inversion, the topological classification is trivial [4, 8].

In case it is odd under inversion, the classification of topological phases with anomalous boundary states is \mathbb{Z}_4 , where odd elements “1”, “3” indicate a first-order topological superconductor hosting a helical Majorana edge mode, and the even element “2” is a second-order topological superconductor hosting Kramers pairs of Majorana corner states on an inversion symmetric sample [4, 8].

The $p + i\tau p$ -wave order parameter in Eq. (31) is spatially modulated [1, 30] such that it is even (odd) under inversion for $\phi = 0$ ($\pi/2$). For other values of ϕ , the system does not respect inversion symmetry. Following the arguments above, this implies that we may find a second-order topological phase hosting Kramers pairs of Majorana corner states only for $\phi = \pi/2$. However, the corner states may persist for a range of ϕ around $\phi = \pi/2$ until the surface gap closes [1, 3, 4]. The s_τ -wave order parameter Eq. (32) is odd under inversion, thus allowing a second-order topological phase.

Symmetry-based indicators are sufficient criteria for topological crystalline phases expressed in terms of symmetry-eigenvalues at a few high-symmetry momenta only. A particular strength of this formalism is that in the weak-pairing limit of an infinitesimal pairing strength $\Delta \rightarrow 0$, the symmetry-based indicator can be expressed in terms of symmetry-data of the normal-state Hamiltonian only. The symmetry-based indicator takes the symmetry of the superconducting order parameter into account, as different symmetry-based indicators are defined depending on the irreducible representation of the order parameter. This allows one to formulate sufficient criteria for the topology of a superconducting phase depending on the pairing symmetry and band structure data of the normal state.

The symmetry-based indicator for the second-order topological phase with inversion symmetry \mathcal{I} and pairing symmetry $u(\mathcal{I})\Delta(-k_x, -k_y)u^T(\mathcal{I}) = -\Delta(k_x, k_y)$ has been calculated as [5]

$$z_2 = \mathfrak{N}_+^\Gamma - \mathfrak{N}_+^M \pmod{4} \quad (34)$$

where $\mathfrak{N}_+^{\mathbf{k}_s}$ is the number of Kramers pairs of eigenstates of the BdG Hamiltonian with negative energy and even inversion eigenvalue +1

at the inversion symmetric momenta $\mathbf{k}_s = \Gamma, M$. Here, we used that sixfold rotation symmetry relates the three M points in the hexagonal Brillouin zone, such that $\mathfrak{N}_+^M = \mathfrak{N}_+^{M_1} = \mathfrak{N}_+^{M_2} = \mathfrak{N}_+^{M_3}$. For the symmetry-based indicator, $z_2 = 1, 3$ corresponds to a first-order topological superconductor with a helical Majorana edge state, and $z_2 = 2$ corresponds to the second-order topological superconductor. In the weak pairing limit of an infinitesimal order parameter $\Delta \rightarrow 0$, we can express the symmetry-based indicator in terms of the symmetry-data of the normal-state Hamiltonian only:

$$z_2^{\text{WP}} = n_+^\Gamma|_{\text{occ}} + n_-^\Gamma|_{\text{unocc}} - n_+^M|_{\text{occ}} - n_-^M|_{\text{unocc}} \pmod{4} \quad (35)$$

where $n_\pm^{\mathbf{k}_s}|_{\text{occ}}$ ($n_\pm^{\mathbf{k}_s}|_{\text{unocc}}$), are the occupied (unoccupied) Kramers pairs of bands with inversion parity ± 1 at the high-symmetry momentum $\mathbf{k}_s = \Gamma, M$. It is notable that this formula does not depend on the properties of the low-energy theory at the K, K' points.

s_τ pairing. First, we evaluate the weak-pairing limit of the symmetry-based indicator for s_τ -wave pairing. At the points Γ, M , the energy of the bands is of the order of the nearest neighbour hopping t , which is our largest energy scale, $t \gg t', \mu, \Delta$. This allows one to neglect spin-orbit coupling when computing the inversion parities of the occupied and unoccupied bands. Without spin-orbit coupling, the Bloch Hamiltonian for the nearest neighbour hopping can be written as

$$h_0(\mathbf{k}) = ts_0 \begin{pmatrix} 0 & 1 + e^{-i\mathbf{a}_1\mathbf{k}} + e^{-i\mathbf{a}_2\mathbf{k}} \\ 1 + e^{i\mathbf{a}_1\mathbf{k}} + e^{i\mathbf{a}_2\mathbf{k}} & 0 \end{pmatrix}_\sigma \quad (36)$$

where we wrote the 2×2 matrix in sublattice space σ explicitly. Together with the representation of inversion symmetry, Eq. 33, we find by simultaneously diagonalising $h_0(\mathbf{k})$ and $u(\mathcal{I}; \mathbf{k})$ for the number of Kramers pairs resolved by their inversion parity $n_+^\Gamma|_{\text{occ}} = 0$, $n_-^\Gamma|_{\text{unocc}} = 0$, $n_+^M|_{\text{occ}} = 1$, $n_-^M|_{\text{unocc}} = 1$, such that $z_2^{\text{WP}} = 2$. Taking into account that the s_τ pairing opens a full excitation gap, the onset of this pairing instability is a second-order topological superconducting phase.

$p + i\tau p$ pairing. Due to the spatial modulation of the $p + i\tau p$ superconducting order parameter, the Dirac cones at the K and K' points get folded onto the Γ point. For finite hole doping, the chemical potential lies inside the valence band. Taking the band folding into account, we find $n_+^\Gamma|_{\text{occ}} = 0$, $n_-^\Gamma|_{\text{unocc}} = 2$, $n_+^M|_{\text{occ}} = 2$, $n_-^M|_{\text{unocc}} = 2$ such that $z_2^{\text{WP}} = 2$. As the $p + i\tau p$ pairing instability opens a full gap in the spectrum that is odd under inversion for $\phi = \pi/2$, it leads to a second-order topological phase for $\phi = \pi/2$.

B. Exact diagonalisation results

We now present exact diagonalisation results, for which we have employed a simplified lattice model which accounts only for pairing between the closest sites for which the gap is nonvanishing. For the intervalley $p + ip$ spin triplet phase

$$\mathcal{H}_\Delta = \sum_{\langle \mathbf{R}, \mathbf{R}' \rangle} \Delta(\mathbf{R}, \mathbf{R}') c_{\mathbf{R}, \uparrow}^\dagger c_{\mathbf{R}', \downarrow}^\dagger$$

$$\Delta(\mathbf{R}, \mathbf{R}') = \begin{cases} \Delta' e^{i(\theta - \frac{\pi}{2})} & \mathbf{R}' \in A \\ \Delta' e^{i(\theta + \frac{\pi}{2})} & \mathbf{R}' \in B \end{cases} \quad (37)$$

where θ is the hopping direction.

For the intervalley s_τ spin triplet phase, we find that pairing vanishes exactly between nearest neighbours, thus we consider only pairing between next nearest neighbours,

$$\mathcal{H}_\Delta = \sum_{\langle\langle \mathbf{R}, \mathbf{R}' \rangle\rangle} \Delta(\mathbf{R}, \mathbf{R}') c_{\mathbf{R}, \uparrow}^\dagger c_{\mathbf{R}', \downarrow}^\dagger$$

$$\Delta(\mathbf{R}, \mathbf{R}') = \begin{cases} +\Delta' & \theta = 0, \pm \frac{2\pi}{3} \\ -\Delta' & \theta = \pi, \pm \frac{\pi}{3} \end{cases} \quad (38)$$

For the intravalley $p + i\tau p$ spin triplet phase, we consider pairing between nearest neighbors,

$$\mathcal{H}_\Delta = \frac{1}{2} \sum_{\langle \mathbf{R}, \mathbf{R}' \rangle} \Delta(\mathbf{R}, \mathbf{R}') (e^{i\phi_s} c_{\mathbf{R}, \uparrow}^\dagger c_{\mathbf{R}', \uparrow}^\dagger + e^{-i\phi_s} c_{\mathbf{R}, \downarrow}^\dagger c_{\mathbf{R}', \downarrow}^\dagger)$$

$$\Delta(\mathbf{R}, \mathbf{R}') = \begin{cases} +\Delta' & \mathbf{R}' \in A \\ -\Delta' & \mathbf{R}' \in B \end{cases} \quad (39)$$

For the intervalley s_τ and $p + ip$ spin triplet phases, we may write the Bogoliubov-de Gennes Hamiltonian in matrix form as

$$\mathcal{H}_{\text{nor.}} + \mathcal{H}_\Delta = \frac{1}{2} \sum_{\mathbf{R}, \mathbf{R}'} \begin{pmatrix} c_{\mathbf{R}, \uparrow}^\dagger & c_{\mathbf{R}, \downarrow} \end{pmatrix} \begin{pmatrix} H_{\uparrow\uparrow}(\mathbf{R}, \mathbf{R}') & \Delta_{\uparrow\downarrow}(\mathbf{R}, \mathbf{R}') \\ \Delta_{\downarrow\uparrow}(\mathbf{R}, \mathbf{R}') & -H_{\downarrow\downarrow}^*(\mathbf{R}, \mathbf{R}') \end{pmatrix} \begin{pmatrix} c_{\mathbf{R}', \uparrow} \\ c_{\mathbf{R}', \downarrow}^\dagger \end{pmatrix} \quad (40)$$

where the normal-state Hamiltonian $\mathcal{H}_{\text{nor.}}$ is defined in Eq. (30).

Similarly, we may write the Bogoliubov-de Gennes Hamiltonian for the intravalley $p + i\tau p$ spin-triplet phase as

$$\mathcal{H}_{\text{nor.}} + \mathcal{H}_\Delta = \frac{1}{2} \sum_{\mathbf{R}, \mathbf{R}', s} \begin{pmatrix} c_{\mathbf{R}, s}^\dagger & c_{\mathbf{R}, s} \end{pmatrix} \begin{pmatrix} H_{s,s}(\mathbf{R}, \mathbf{R}') & \Delta_{s,s}(\mathbf{R}, \mathbf{R}') \\ \Delta_{s,s}^\dagger(\mathbf{R}, \mathbf{R}') & -H_{s,s}^*(\mathbf{R}, \mathbf{R}') \end{pmatrix} \begin{pmatrix} c_{\mathbf{R}', s} \\ c_{\mathbf{R}', s}^\dagger \end{pmatrix} \quad (41)$$

Here the two blocks with opposite s_z eigenvalue are related by time-reversal symmetry $\mathcal{T} = is_y K$, while each block separately satisfies particle-hole symmetry. The block-diagonal form allows us to

perform the exact diagonalisation in only one of the two spin blocks, and infer the results in the other block by its relation required by time-reversal symmetry or particle-hole antisymmetry.

We plot the spectrum of infinite superconducting ribbons in the intervalley s_τ , intravalley $p + i\tau p$ and intervalley $p + ip$ spin triplet phases in Figs. 5, 6, 8, as a function of momentum k along the ribbon respectively. We observe anomalous edge features in all three cases. In most cases, the 1D dispersion of modes propagating along opposite edges is split, and the lines of different color and thickness indicate opposite edge modes.

To demonstrate the second-order topology of the intervalley s_τ and intravalley $p + i\tau p$ spin triplet phases, we show the wavefunction profile of the six lowest energy eigenstates forming the Majorana corner modes on a hexagonal flake geometry, and corresponding spectrum in Figs. 5 and 6. The exact diagonalisation of the BdG Hamiltonians was performing within a spin-block for both intervalley s_τ and intravalley $p + i\tau p$ spin-triplet phases, c.f. Eqs. (40) and (41), so the Majorana corner modes in both cases have a degenerate Kramers partner in the opposite spin block.

For the intervalley s_τ spin triplet phase, in which pairing occurs between opposite spins, we plot the spectrum of the non-redundant BdG Hamiltonian, so that each energy eigenvalue corresponds to a quasiparticle whose antiparticle is identical to its Kramers partner. Decomposing each zero energy mode into two Majorana modes, we find one Majorana Kramers pair at each corner which are protected by time-reversal symmetry. Two gapless counterpropagating modes are observed on each edge for the armchair geometry, but we find no edge states for the zigzag geometry, as shown in Fig. 5. On the flake geometry, Majorana corner states appear on corners between zigzag edges. The Majorana corner modes are a signature of the intrinsic second-order topology of the crystalline bulk superconductor, because these corner modes can not be removed without breaking the symmetries or closing the bulk gap [4].

For the intravalley $p + i\tau p$ phase, in which pairing occurs for equal spins, we plot the spectrum for the BdG Hamiltonian within a single spin block, so that each energy eigenvalue corresponds to a quasiparticle with a Kramers partner in the opposite spin block. For a hexagonal flake with an armchair boundary, at $\phi = \pi/2$, we find one Majorana Kramers pair at each corner of the flake, protected by time-reversal symmetry. These results confirm the existence of a second-order topology which we concluded in the previous section via the symmetry-based indicators. We observe gapless counterpropagating modes along each edge for the zigzag geometry, however the

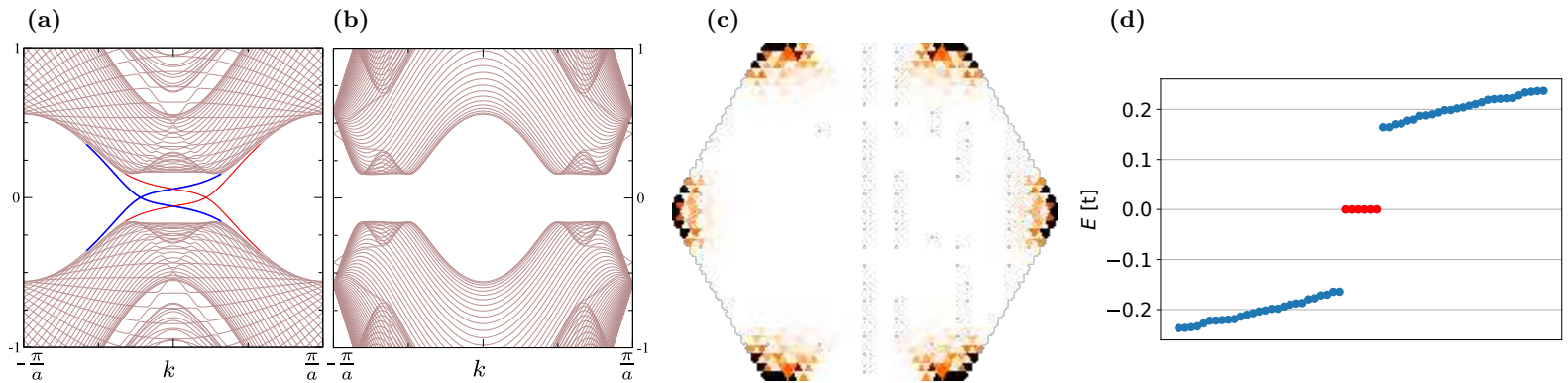


FIG. 5: Exact diagonalisation results for the second-order topological s_7 spin triplet phase. (a), (b) The 1D dispersion of infinite superconducting ribbons with (a) armchair and (b) zigzag terminations. Edge modes propagating along opposite edges are shown in different colors. (c) Wavefunction profile of the six zero energy eigenstates on a flake geometry. These are the subgap states marked in red in the corresponding spectrum displaying 60 eigenstates around zero in (d). Here we use the parameters $\eta = 0.2t$, $\mu = 0.4t$, $\Delta' = 0.033t$ corresponding to a bulk superconducting gap $\Delta \approx 0.16t$.

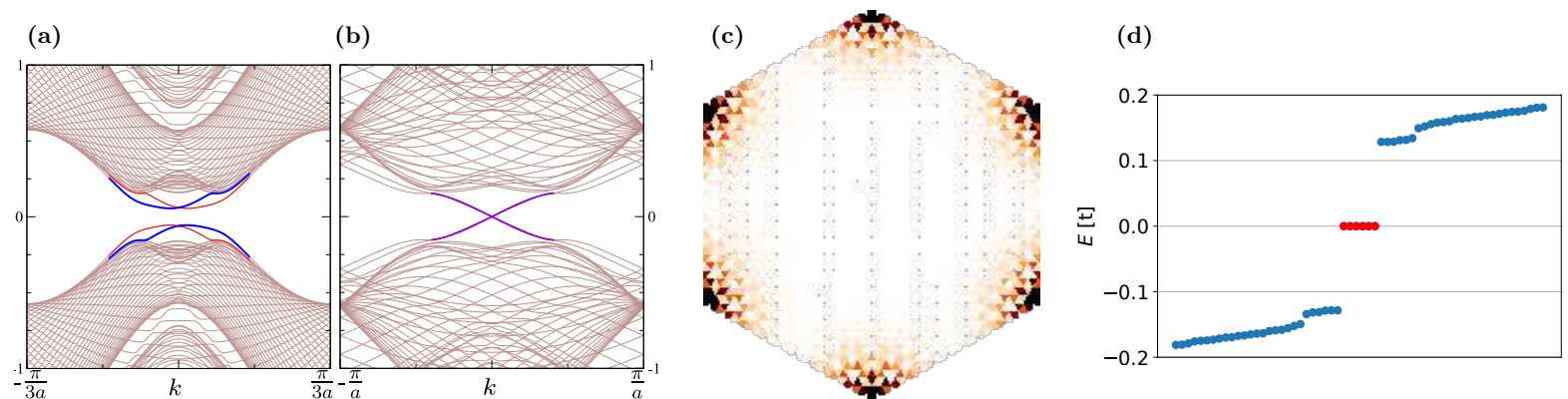


FIG. 6: Exact diagonalisation results for the second-order topological $p + i7p$ intravalley spin triplet phase. (a), (b), The 1D dispersion of infinite superconducting ribbons with (a) armchair and (b) zigzag terminations. Edge modes propagating along opposite edges are shown in different colors. (c) Wavefunction profile of the six lowest absolute energy eigenstates on a flake geometry. These are the subgap states marked in red in the corresponding spectrum displaying 60 eigenenergies around zero in (d). Here we use the parameters $\eta = 0.2t$, $\mu = 0.4t$, $\Delta' = 0.13t$, and $\phi = \pi/2$ corresponding to a bulk superconducting gap $\Delta \approx 0.16t$.

772 edge behavior for an armchair ribbon is sensitive to the width of the
 773 ribbon as well as the value of the pair density wave order parameter
 774 ϕ , as shown in Fig. 6. Both the armchair ribbon and flake have
 775 a width of 35 unit cells. In this case, the plotted ribbon disper-
 776 sion with armchair edges is gapped, and the flake exhibits Kramers
 777 pairs of Majorana corner states on corners between armchair edges
 778 at $\phi = \pi/2$. For $\phi = \pi/2$, the flake is inversion symmetric and the
 779 zero energy corner modes are a signature of the intrinsic second-order
 780 topology of the bulk superconductivity [1, 4].

781 The behavior of edge modes exhibits a threefold periodicity in

782 the ribbon width. In Fig. 7 we show the level spectrum at $k = 0$
 783 as a function of ϕ for an armchair ribbon of various widths, (a)
 784 35, (b) 36, (c) 37 unit cells. In all cases, the modes propagating
 785 along the left and right edges have distinct 1D dispersions, except at
 786 values $\phi = n\pi/2$, with $n \in \mathbb{Z}$ for which the gap function $\Delta(\mathbf{R}, \mathbf{R}')$
 787 is reflection symmetric about the center of the ribbon. We find that
 788 the edge is always gapped at $\phi = \pi/2$, when $\Delta(\mathbf{R}, \mathbf{R}')$ is odd under
 789 inversion. At $\phi = 0$, the gap function is even under inversion and
 790 no higher-order topology is possible. The edge gap closes for a value
 791 of ϕ between $\phi = 0$ and $\phi = \pi/2$, corresponding to the transition at

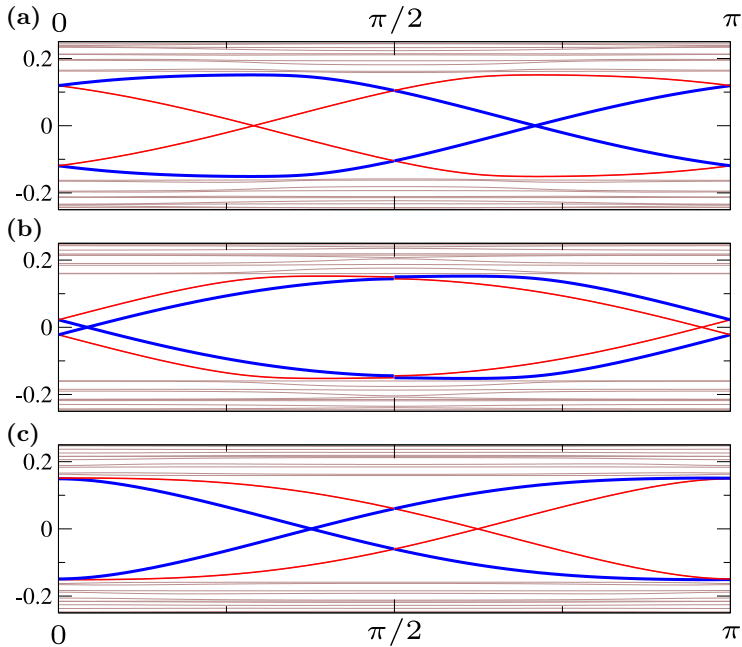


FIG. 7: Dependence of the spectrum (in units of t) on the pair density wave order parameter ϕ in the $p + i\tau p$ state, for ribbons of various width. The energy spectrum at $k = 0$ of an infinite superconducting ribbon with armchair termination of width (a) 35, (b) 36, (c) 37 unit cells as a function of ϕ , for parameters $\eta = 0.2t$, $\mu = 0.4t$ and $\Delta' = 0.13t$ corresponding to a bulk superconducting gap $\Delta \approx 0.16t$.

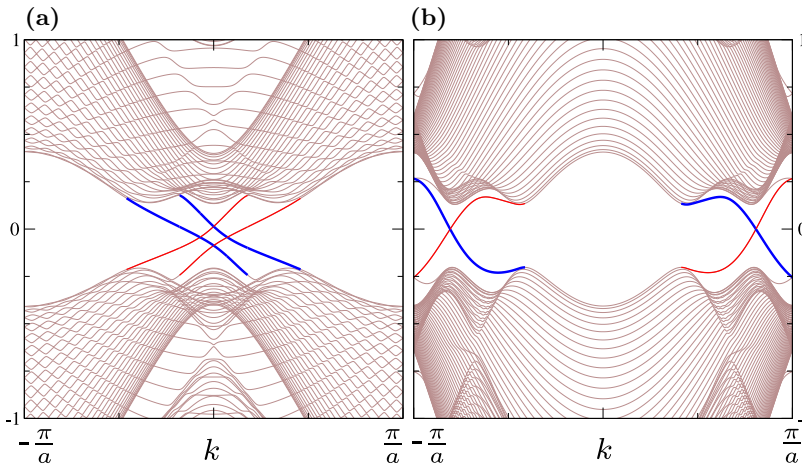


FIG. 8: The 1D dispersion of infinite superconducting ribbons with (a) armchair and (b) zigzag terminations in the $p + i\tau p$ intervalley spin triplet phase, with parameters $\eta = 0.2t$, $\mu = 0.4t$, and $\Delta' = 0.2t$ corresponding to a bulk superconducting gap $\Delta \approx 0.18t$. Edge modes propagating along opposite edges are shown in different colors.

792 which the Majorana corner modes disappear.

793 For the intervalley $p + ip$ spin triplet phase, two co-propagating
794 modes are observed on each edge for both the armchair and zigzag
795 geometries, as illustrated in Fig. 8. Keeping in mind that these
796 modes have been obtained from the BdG Hamiltonian in the form
797 of Eq. (40), the chiral edge modes are Dirac fermions, i.e. they are
798 not their own antiparticle.

VIII. DISCUSSION

800 In this paper we considered the phase diagram of an interacting
801 artificial honeycomb superlattice, with Fermi pockets around the
802 Dirac K , K' points, subject to intrinsic spin-orbit coupling, i.e. a
803 doped two-dimensional topological insulator.

804 We have shown that first and second-order topological supercon-
805 ductivity arises purely due to the Coulomb repulsion, an effect which
806 is enhanced in the limit of localised atomic orbitals.

807 The mechanism has been elucidated for general lattice models with
808 C_{6v} point group symmetry, $SU(2)$ spin rotation and time-reversal
809 symmetry in [1], and is extended here in two ways: (i) the influ-
810 ence of intrinsic spin-orbit coupling is incorporated, breaking spin
811 $SU(2) \rightarrow U(1)$ generating a \mathbb{Z}_2 topological bandgap, and (ii) micro-
812 scopic modeling for a specific, experimentally promising, material is
813 presented. However, while our field theory treatment is generic, we
814 present results specifically for a model of an artificial honeycomb lat-
815 tice based on a nanopatterned hole-doped semiconductor quantum
816 well, having in mind the fact that in this situation there is a high
817 degree of experimental control over the electron-electron interaction
818 as well as the band structure.

819 Our microscopic modeling shows that three distinct (first and
820 second-order) topological superconducting phases emerge for real-
821 istic material parameters, and moreover, that these instabilities are
822 the leading weak coupling instabilities of the Fermi surface – with
823 magnetic and charge ordering only setting in at larger interaction
824 strengths. The superconducting phases are:

- 825 1. $p + ip$ intervalley, which admits a first-order topological in-
826 variant and therefore hosts gapless chiral edge modes; we have
827 shown from numerical calculations that this phase hosts two
828 co-propagating chiral Dirac fermionic edge modes.
- 829 2. $p + i\tau p$ intravalley, a spatially modulated pair density wave
830 which hosts two Majorana edge modes of opposite chirality
831 due to the opposite pairing in the two valleys. Hybridization

of the edge modes may give rise the Kramers pairs of Majorana corner modes. We have confirmed the corresponding second-order topology of the bulk superconductor for $\phi = \pi/2$, where ϕ is the phase of the pair density wave, using an argument from symmetry-based indicators in addition to our exact diagonalisation results.

3. s_τ intervalley, which is also second-order topological, but with a bulk order that has a different spatial structure to the $p + i\tau p$ state. It is interesting to note that despite the s -wave nature of the s_τ state, the phase exhibits nontrivial higher-order topology. This is due to the fact that while the gap is s -wave, it has different signs on the two Fermi surfaces at each valley, since the gap is proportional to τ_y .

The boundary physics of the superconducting state could be probed in experiment through STM [22], or through measurements of the Josephson critical current [23]. It has been proposed that higher-order topological superconductors host Majorana states at disinclinations and defects [25–29], a phenomenon currently unexplored experimentally, which could offer another signature of higher-order topology.

Very recent progress in n -type semiconductors patterned with a honeycomb superlattice [46–48] has clearly demonstrated Dirac band structure features. Our findings show that p -type semiconductor patterned with a honeycomb superlattice is an enticing avenue towards topological superconducting phases. The p -type semiconductor allows for strong intrinsic spin-orbit coupling, which is otherwise negligible in n -type. Stronger spin-orbit coupling reduces the effective

Dirac velocity, flattening the bands and enhancing interaction effects compared to the n -type scenario. We find that having spin-orbit coupling as an additional handle, we are more readily able to realise the necessary conditions for the pairing mechanism discussed here.

Other superconducting superlattice systems in which intrinsic spin-orbit coupling is present include, e.g. twisted transition metal dichalogenides [55], and $\text{Ba}_6\text{Nb}_{11}\text{S}_{28}$ [57]. Non-superlattice materials featuring superconductivity and Dirac physics, localised orbitals and spin-orbit coupling include $\text{Pb}_{1/3}\text{TaS}_2$ [58], few-layer stanene [59], monolayer TMDs [60–64], doped topological insulators [65–73], and recently discovered vanadium-based kagome metals [74–93]. Many of these systems exhibit superconductivity at relatively low carrier densities, and a phase diagram as a function of density similar to the one predicted here. It is our hope that the present study offers a new perspective on the results of these experiments, and suggests new directions to explore.

ACKNOWLEDGEMENTS

H. D. Scammell acknowledges funding from ARC Centre of Excellence FLEET. MG acknowledges support by the European Research Council (ERC) under the European Union’s Horizon 2020 research and innovation program under grant agreement No. 856526, and from the Deutsche Forschungsgemeinschaft (DFG) Project Grant 277101999 within the CRC network TR 183 ”Entangled States of Matter” (subproject A03 and C01), and from the Danish National Research Foundation, the Danish Council for Independent Research — Natural Sciences.

-
- [1] T. Li, M. Geier, J. Ingham and H. D. Scammell, “Higher-order topological superconductivity from repulsive interactions in kagome and honeycomb systems”, [arXiv:2108.10897 \[cond-mat.supr-con\]](https://arxiv.org/abs/2108.10897).
 - [2] Y. Peng, Y. Bao, and F. von Oppen, “Boundary Green functions of topological insulators and superconductors”, *Phys. Rev. B* **95**, 235143 (2017).
 - [3] J. Langbehn, Y. Peng, L. Trifunovic, F. von Oppen and P. W. Brouwer, “Reflection symmetric second-order topological insulators and superconductors”, *Phys. Rev. Lett.* **119**, 246401 (2017).
 - [4] M. Geier, L. Trifunovic, M. Hoskam and P. W. Brouwer, “Second-order topological insulators and superconductors with an order-two crystalline symmetry”, *Phys. Rev. B* **97**, 205135 (2018).
 - [5] M. Geier, P. W. Brouwer and L. Trifunovic, “Symmetry-based indicators for topological Bogoliubov-de Gennes Hamiltonians”, *Phys. Rev. B* **101**, 245128 (2020).
 - [6] K. Shiozaki, “Variants of the symmetry-based indicator”, [arXiv:1907.13632 \[cond-mat.mes-hall\]](https://arxiv.org/abs/1907.13632).
 - [7] S. Ono, H.-C. Po and H. Watanabe, “Refined symmetry indicators for topological superconductors in all space groups”, *Sci. Adv.* **6**, eaaz8367 (2020).
 - [8] L. Trifunovic and P. W. Brouwer, “Higher-order bulk-boundary correspondence for topological crystalline phases”, *Phys. Rev. X* **9**, 011012 (2019).

- [9] L. Trifunovic and P. W. Brouwer, “Higher-order topological band structures”, *Physica Status Solidi (B)*, 2020.
- [10] E. Khalaf, “Higher-order topological insulators and superconductors protected by inversion symmetry”, *Phys. Rev. B* **97**, 205136 (2018).
- [11] S.-B. Zhang, W. B. Rui, A. Calzona, S.-J. Choi, A. P. Schnyder, B. Trauzettel, “Topological and holonomic quantum computation based on second-order topological superconductors,” *Phys. Rev. Research* **2**, 043025 (2020).
- [12] R.-X. Zhang et al., “higher-order Topology and Nodal Topological Superconductivity in Fe(Se,Te) Heterostructures”, *Phys. Rev. Lett.* **123**, 167001 (2019).
- [13] X. Zhu, “Second-order Topological Superconductors with Mixed Pairing”, *Phys. Rev. Lett.* **122**, 236401 (2019).
- [14] S. Franca, D. V. Efremov and I. C. Fulga, “Phase tunable second-order topological superconductor”, *Phys. Rev. B* **100**, 075415 (2019).
- [15] Z. Wu, Z. Yan and W. Huang, “Higher-order topological superconductivity: possible realization in Fermi gases and Sr_2RuO_4 ”, *Phys. Rev. B* **99**, 020508 (2019).
- [16] B. Roy, “Higher-order topological superconductors in \mathcal{P} -, \mathcal{T} -odd quadrupolar Dirac materials”, *Phys. Rev. B* **101**, 220506 (2020).
- [17] J. Ahn and B.-J. Yang, “Higher-Order Topological Superconductivity of Spin-Polarized Fermions” *Phys. Rev. Research* **2**, 012060 (2020).
- [18] R.-X. Zhang and S. Das Sarma, “Intrinsic Time-reversal-invariant Topological Superconductivity in Thin Films of Iron-based Superconductors”, *Phys. Rev. Lett.* **126**, 137001 (2021).
- [19] A. Chew et al., “Higher-Order Topological Superconductivity in Twisted Bilayer Graphene”, [arXiv:2108.05373 \[cond-mat.supr-con\]](https://arxiv.org/abs/2108.05373).
- [20] Y.-T. Hsu et al., “Inversion-protected higher-order topological superconductivity in monolayer WTe_2 ”, *Phys. Rev. Lett.* **125**, 097001 (2020).
- [21] Y. Wang, M. Lin and T. L. Hughes, “Weak-pairing higher-order topological superconductors,” *Phys. Rev. B* **98**, 165144 (2018).
- [22] M. J. Gray et al., “Evidence for Helical Hinge Zero Modes in an Fe-Based Superconductor”, *Nano Lett.* **19**, 4890 (2019).
- [23] Y.-B. Choi et al., “Evidence of higher-order topology in multilayer WTe_2 from Josephson coupling through anisotropic hinge states”, *Nat. Mater.* **19**, 974–979 (2020).
- [24] F. Schindler et al., “Higher-order topology in bismuth”, *Nat. Phys.* **14**, 918–924 (2018).
- [25] J. C. Y. Teo and T. L. Hughes, “Existence of Majorana-Fermion Bound States on Disclinations and the Classification of Topological Crystalline Superconductors in Two Dimensions”, *Phys. Rev. Lett.* **111**, 047006 (2013).
- [26] W. A. Benalcazar, J. C. Y. Teo, and T. L. Hughes, “Classification of two-dimensional topological crystalline superconductors and Majorana bound states at disclinations”, *Phys. Rev. B* **89**, 224503 (2014).
- [27] X. Zhu, “Tunable Majorana corner states in a two-dimensional second-order topological superconductor induced by magnetic fields”, *Phys. Rev. B* **97**, 205134 (2018).
- [28] M. Geier, I. C. Fulga and A. Lau, “Bulk-boundary-defect correspondence at disclinations in rotation-symmetric topological insulators and superconductors”, *SciPost Phys.* **10**, 092 (2021).
- [29] B. Roy and V. Juričić, “Dislocation as a bulk probe of higher-order topological insulators”, *Phys. Rev. Research* **3**, 033107 (2021).
- [30] T. Li, J. Ingham and H. D. Scammell, “Artificial Graphene: Unconventional Superconductivity in a Honeycomb Superlattice”, *Phys. Rev. Research* **2**, 043155 (2020).
- [31] M. Polini et al., “Artificial honeycomb lattices for electrons, atoms and photons”, *Nat. Nano* **8**, 625–633 (2013).
- [32] I. Bloch, J. Dalibard and W. Zwerger, “Many-body physics with ultracold gases”, *Rev. Mod. Phys.* **80**, 885 (2008).
- [33] D.-W. Zhang et al., “Topological quantum matter with cold atoms”, *Adv. Phys.* **67**, 253-402 (2018).
- [34] N. R. Cooper, J. Dalibard and I. B. Spielman, “Topological Bands for Ultracold Atoms”, *Rev. Mod. Phys.* **91**, 015005 (2019).
- [35] A. Browaeys and T. Lahaye, “Many-body physics with individually controlled Rydberg atoms”, *Nat. Phys.* **16**, 132-142 (2020).
- [36] Y. Cao et al., “Unconventional superconductivity in magic-angle graphene superlattices”, *Nature* **556**, 43–50 (2018)
- [37] Y. Cao et al., “Correlated Insulator Behaviour at Half-Filling in Magic Angle Graphene Superlattices”, *Nature* **556**, 80–84 (2018).
- [38] H. Yoo et al., “Atomic and electronic reconstruction at the van der Waals interface in twisted bilayer graphene”, *Nat. Mater.* **18**, 448-453 (2019).
- [39] A. Weston et al., “Atomic reconstruction in twisted bilayers of transition metal dichalcogenides”, *Nat. Nano* **15**, 592–597 (2020).
- [40] A. K. Geim and I. V. Grigorieva, “Van der Waals heterostructures”, *Nature* **499**, 419–425 (2013).
- [41] P. Ajayan, P. Kim and K. Banerjee, “Two-dimensional van der Waals materials”, *Physics Today* **69**, 9, 38 (2016).
- [42] C. Forsythe et al., “Band structure engineering of 2D materials using patterned dielectric superlattices”, *Nat. Nano.* **13**, 566–571 (2018).
- [43] C.-H. Park and S. G. Louie, “Making Massless Dirac Fermions from Patterned Two-Dimensional Electron Gases”, *Nano Lett.* **9**, 1793-1797 (2009).
- [44] M. Gibertini et al., “Engineering artificial graphene in a two-dimensional electron gas”, *Phys. Rev. B* **79**, 241406(R) (2009).
- [45] A. Singha et al., “Two-dimensional Mott-Hubbard electrons in an artificial honeycomb lattice”, *Science* **332**, 1176 (2011).
- [46] S. Weng et al., “Observation of Dirac bands in artificial graphene in small-period nanopatterned GaAs quantum wells”, *Nature Nano.* **13**, 29–33 (2018).
- [47] L. Du et al., “Emerging many-body effects in semiconductor artificial graphene with low disorder”, *Nature Comm.* **9**, 3299 (2018).

- [48] L. Du et al., “Observation of flat bands in gated semiconductor artificial graphene”, *Phys. Rev. Lett.* **126**, 106402 (2021).
- [49] O. A. Tkachenko, V. A. Tkachenko, I. S. Terekhov and O. P. Sushkov, “Effects of Coulomb screening and disorder on an artificial graphene based on nanopatterned semiconductor”, *2D Mater.* **2**, 014010 (2015).
- [50] T. Li and O. P. Sushkov, “Chern insulating state in laterally patterned semiconductor heterostructures”, *Phys. Rev. B* **94**, 155311 (2016).
- [51] T. Li and O. P. Sushkov, “Two-dimensional topological semimetal state in a nanopatterned semiconductor system”, *Phys. Rev. B* **96**, 085301 (2017).
- [52] O. P. Sushkov and A. H. Castro Neto, “Topological Insulating States in Laterally Patterned Ordinary Semiconductors”, *Phys. Rev. Lett.* **110**, 186601 (2013).
- [53] H. D. Scammell and O. P. Sushkov, “Tuning the topological insulator states of artificial graphene”, *Phys. Rev. B* **99**, 085419 (2019).
- [54] C. L. Kane and E. J. Mele, “Quantum Spin Hall Effect in Graphene”, *Phys. Rev. Lett.* **95**, 226801 (2005).
- [55] L. Wang et al., “Correlated electronic phases in twisted bilayer transition metal dichalcogenides”, *Nature Materials* **19**, 861 (2020).
- [56] F. Wu, T. Lovorn, E. Tutuc, I. Martin and A. H. MacDonald, “Topological insulators in twisted transition metal dichalcogenide homobilayers”, *Phys. Rev. Lett.* **122**, 086402 (2019).
- [57] A. Devarakonda et al., “Clean 2D superconductivity in a bulk van der Waals superlattice”, *Science* **370**, 231-236 (2020).
- [58] X. Yang et al., “Anisotropic superconductivity in topological crystalline metal $\text{Pb}_{1/3}\text{TaS}_2$ with multiple Dirac fermions”, *Phys. Rev. B* **104**, 035157 (2021).
- [59] M. Liao et al., “Superconductivity in few-layer stanene” *Nat. Phys.* **14**, 344–348 (2018).
- [60] S. C. de la Barrera et al., “Tuning Ising superconductivity with layer and spin-orbit coupling in two-dimensional transition-metal dichalcogenides”, *Nat. Comm.* **9**, 1427 (2018).
- [61] J. Lu et al., “Full superconducting dome of strong Ising protection in gated monolayer WS_2 ”, *Proc. Natl. Acad. Sci. U.S.A.* **115** (14) 3551-3556 (2018).
- [62] J. Lu et al., “Evidence for two-dimensional Ising superconductivity in gated MoS_2 ”, *Science* **350**, 6266 1353-1357 (2015).
- [63] Y. Yang et al., “Enhanced superconductivity upon weakening of charge density wave transport in 2H-TaS₂ in the two-dimensional limit”, *Phys. Rev. B* **98**, 035203 (2018).
- [64] J. T. Ye et al., “Superconducting Dome in a Gate-Tuned Band Insulator”, *Science* **338**, 1193-1196 (2012).
- [65] S. Yonezawa, “Nematic Superconductivity in Doped Bi_2Se_3 Topological Superconductors” *Condens. Matter* **4**(1), 2 (2019).
- [66] M. Kreiner et al., “Bulk Superconducting Phase with a Full Energy Gap in the Doped Topological Insulator $\text{Cu}_x\text{Bi}_2\text{Se}_3$ ”, *Phys. Rev. Lett.* **106**, 127004 (2011).
- [67] S. Sasaki et al., “Odd-Parity Pairing and Topological Superconductivity in a Strongly Spin-Orbit Coupled Semiconductor”, *Phys. Rev. Lett.* **109**, 217004 (2012).
- [68] Z. Liu et al., “Superconductivity with Topological Surface State in $\text{Sr}_x\text{Bi}_2\text{Se}_3$ ”, *J. Am. Chem. Soc.* **137**, 10512–10515 (2015).
- [69] T. Sato et al., “Fermiology of Strongly Spin-Orbit Coupled Superconductor $\text{Sn}_{1-x}\text{In}_x\text{Te}$ and its Implication to Topological Superconductivity”, *Phys. Rev. Lett.* **110**, 206804 (2013).
- [70] M. Novak et al., “Unusual nature of fully-gapped superconductivity in In-doped SnTe ”, *Phys. Rev. B* **88**, 140502 (2013).
- [71] L. Fu and E. Berg, “Odd-Parity Topological Superconductors: Theory and Application to $\text{Cu}_x\text{Bi}_2\text{Se}_3$ ”, *Phys. Rev. Lett.* **105**, 097001 (2010).
- [72] V. Fatemi et al., “Electrically tunable low-density superconductivity in a monolayer topological insulator”, *Science* **362** 6417 926-929 (2018).
- [73] E. Sajadi et al., “Gate-induced superconductivity in a monolayer topological insulator”, *Science* **362** 6417 922-925 (2018).
- [74] B. R. Ortiz et al., “ CsV_3Sb_5 : A \mathbb{Z}_2 Topological Kagome Metal with a Superconducting Ground State”, *Phys. Rev. Lett.* **125**, 247002 (2020).
- [75] C. C. Zhu et al., “Double-dome superconductivity under pressure in the V-based Kagome metals AV_3Sb_5 ($A = \text{Rb}$ and K)”, <https://arxiv.org/abs/2104.14487>.
- [76] K. Y. Chen et al., “Double Superconducting Dome and Triple Enhancement of T_c in the Kagome Superconductor CsV_3Sb_5 under High Pressure”, *Phys. Rev. Lett.* **126**, 247001 (2021).
- [77] B. R. Ortiz et al., “Superconductivity in the \mathbb{Z}_2 kagome metal KV_3Sb_5 ”, *Phys. Rev. Materials* **5**, 034801 (2021).
- [78] S. Ni et al., “Anisotropic superconducting properties of Kagome metal CsV_3Sb_5 ”, *Chin. Phys. Lett.* **38** 057403 (2021).
- [79] H. Chen et al., “Roton pair density wave and unconventional strong-coupling superconductivity in a topological kagome metal”, *Phys. Rev. X* **11**, 031026 (2021).
- [80] Z. Liang et al., “Three-dimensional charge density wave and robust zero-bias conductance peak inside the superconducting vortex core of a kagome superconductor CsV_3Sb_5 ” *Phys. Rev. X* **11**, 031026 (2021).
- [81] J. Zhao, “Electronic correlations in the normal state of the kagome superconductor KV_3Sb_5 ”, *Phys. Rev. B* **103**, L241117 (2021).
- [82] M. Kang et al., “Twofold van Hove singularity and origin of charge order in topological kagome superconductor CsV_3Sb_5 ”, [arXiv:2105.01689 \[cond-mat.str-el\]](https://arxiv.org/abs/2105.01689).
- [83] Y.-X. Jiang et al., “Unconventional chiral charge order in kagome superconductor KV_3Sb_5 ”, *Nat. Mater.* (2021).
- [84] H. Li et al., “Rotation symmetry breaking in the normal state of a kagome superconductor KV_3Sb_5 ”, [arXiv:2104.08209 \[cond-mat.supr-con\]](https://arxiv.org/abs/2104.08209).

- [85] B. R. Ortiz et al., “New kagome prototype materials: discovery of KV_3Sb_5 , RbV_3Sb_5 , and CsV_3Sb_5 ” *Phys. Rev. Mat.* **3**, 094407 (2019).
- [86] H. Zhao et al., “Cascade of correlated electron states in a kagome superconductor CsV_3Sb_5 ” [arXiv:2103.03118 \[cond-mat.supr-con\]](#).
- [87] H. X. Li et al., “Observation of Unconventional Charge Density Wave without Acoustic Phonon Anomaly in Kagome Superconductors AV_3Sb_5 ($A=Rb,Cs$)” [arXiv:2103.09769 \(2021\)](#).
- [88] T. Qian et al., “Revealing the competition between charge-density wave and superconductivity in CsV_3Sb_5 through uniaxial strain” [arXiv:2107.04545 \(2021\)](#).
- [89] M. H. Christensen et al., “Theory of the charge-density wave in AV_3Sb_5 kagome metals” [arXiv:2107.04546 \[cond-mat.supr-con\]](#).
- [90] H. Tan et al., “Charge density waves and electronic properties of superconducting kagome metals”, *Phys. Rev. Lett.* **127**, 046401 (2021).
- [91] T. Park, M. Ye and L. Balents “Electronic instabilities of kagome metals: saddle points and Landau theory”, *Phys. Rev. B* **104**, 035142 (2021).
- [92] X. Wu et al., “Nature of unconventional pairing in the kagome superconductors AV_3Sb_5 ”, [arXiv:2104.05671 \[cond-mat.supr-con\]](#).
- [93] Y.-P. Lin and R. M. Nandkishore, “Kagome superconductors from Pomeranchuk fluctuations in charge density wave metals”, [arXiv:2107.09050 \[cond-mat.str-el\]](#).
- [94] K. Seo, B. A. Bernevig and J. Hu, “Pairing Symmetry in a Two-Orbital Exchange Coupling Model of Oxypnictides”, *Phys. Rev. Lett.* **101**, 206404 (2008).
- [95] T. Hanaguri, S. Niitaka, K. Kuroki and H. Takagi, “Unconventional s-Wave Superconductivity in $Fe(Se,Te)$ ” *Science* **328** 474-476 (2010).
- [96] P. J. Hirschfeld, M. M. Korshunov, and I. I. Mazin, “Gap symmetry and structure of Fe-based superconductors”, *Rep. Prog. Phys.* **74** 124508 (2011).
- [97] Y. Bang and G. R. Stewart, “Superconducting properties of the s_{\pm} -wave state: Fe-based superconductors”, *J. Phys.: Condens. Matter* **29** 123003 (2017).
- [98] R.-X. Zhang, W. S. Cole and S. Das Sarma, “Helical Hinge Majorana Modes in Iron-Based Superconductors”, *Phys. Rev. Lett.* **122**, 187001 (2019).
- [99] S. Qin, C. Fang, F.-C. Zhang and J. Hu, “Topological Superconductivity in an s-wave Superconductor and Its Implication to Iron-based Superconductors”, [arXiv:2106.04200 \[cond-mat.supr-con\]](#).
- [100] R. Winkler, *Spin-Orbit Coupling Effects in Two-Dimensional Electron and Hole Systems* (Springer-Verlag, Berlin, 2003).
- [101] V. N. Kotov, B. Uchoa and A. H. Castro Neto, “ $1/N$ expansion in correlated graphene”, *Phys. Rev. B* **80**, 165424 (2009).
- [102] X.F. Wang and T. Chakraborty, “Collective excitations of Dirac electrons in a graphene layer with spin-orbit interactions”, *Phys. Rev. B* **75**, 033408 (2007).
- [103] A. Thakur, R. Sachdeva and A. Agarwal, “Dynamical polarizability, screening, and plasmons in one, two, and three dimensional massive Dirac systems”, *J. Phys.: Condens. Matter* **29** 105701 (2016).
- [104] P.K. Pyatkovskiy “Dynamical polarization, screening, and plasmons in gapped graphene”, *J. Phys.: Condens. Matter* **21**, 025506 (2009).
- [105] M. Sigrist, “Introduction to Unconventional Superconductivity”, *AIP Conference Proceedings* **789**, 165 (2005).
- [106] R. Samajdar and M. S. Scheurer, “Microscopic pairing mechanism, order parameter, and disorder sensitivity in moiré superlattices: Applications to twisted double-bilayer graphene”, *Phys. Rev. B* **102**, 064501 (2020)
- [107] A. Altland and M. Zirnbauer, “Nonstandard symmetry classes in mesoscopic normal-superconducting hybrid structures”, *Phys. Rev. B* **55**, 1142 (1997).
- [108] A. P. Schnyder, S. Ryu, A. Furusaki, and A. W. W. Ludwig, “Classification of topological insulators and superconductors in three spatial dimensions”, *Phys. Rev. B* **78**, 195125 (2008).

Appendices

Appendix A: Deriving the Effective Hamiltonian

1. Superlattice potential

For a superlattice placed on top of the 2DHG heterostructure, the superlattice potential has a z dependence,

$$W(\mathbf{r}, z) = 2W_0 \sum_i \cos(\mathbf{G}_i \cdot \mathbf{r}) e^{-(z+z_0)G_0}, \quad (\text{A1})$$

where \mathbf{G}_i are the reciprocal lattice vectors connecting corners of the hexagonal Brillouin zone Figure 1. Here, $z = 0$ is the center of the quantum well and z_0 is the distance from the superlattice to the center of the quantum well. This top-gate superlattice breaks inversion symmetry, but one may argue that parity breaking effects are exponentially suppressed and may be ignored in the regime where $z_0 G \ll 1$. Alternatively, we can envisage placing a superlattice on both the top and bottom gates – preserving parity. This is captured by,

$$W(\mathbf{r}, z) = 2W \sum_i \cos(\mathbf{G}_i \cdot \mathbf{r}) e^{-z_0 G_0} \cosh(z G_0). \quad (\text{A2})$$

Henceforth we remove explicit parity breaking in the superlattice potential, working with the expression given in the main text Eq. (3).

2. Effective Dirac Hamiltonian

We explicitly obtain the effective Dirac Hamiltonian via,

$$(\mathcal{H}_0)_{s,\tau,\sigma;s',\tau',\sigma'} = \langle s, \tau, \sigma, \mathbf{p} | \mathcal{H}_{2DHG+W} | s', \tau', \sigma', \mathbf{p} \rangle, \quad (\text{A3})$$

where the wavefunctions $|s, \tau, \sigma, \mathbf{p}\rangle$ are obtained as an expansion in \mathbf{p} near the Dirac points \mathbf{K}_i . Explicitly, they are

$$\langle \mathbf{r} | s, \tau, \sigma, \mathbf{p} \rangle = \sum_{j=1}^3 \bar{A}_{j,s,\tau} C_{\sigma,j} e^{i\tau \mathbf{K}_j \cdot \mathbf{r}} e^{i\mathbf{p} \cdot \mathbf{r}}, \quad (\text{A4})$$

where

$$\bar{A}_{j,s=\uparrow,\tau} = \begin{pmatrix} a_{3/2}(K_0) \hat{\delta} \\ ia_{1/2}(K_0) \tau e^{i2\pi(j-1)/3} \hat{e} \\ a_{-1/2}(K_0) e^{i4\pi(j-1)/3} \hat{\delta} \\ -ia_{-3/2}(K_0) \tau e^{i2\pi(j-1)} \hat{e} \end{pmatrix}, \quad \bar{A}_{j,s=\downarrow,\tau} = \begin{pmatrix} ia_{-3/2}(K_0) \tau e^{-2\pi(j-1)} \hat{e} \\ a_{-1/2}(K_0) e^{-i4\pi(j-1)/3} \hat{\delta} \\ -ia_{1/2}(K_0) \tau e^{-i2\pi(j-1)/3} \hat{e} \\ a_{3/2}(K_0) \hat{\delta} \end{pmatrix}, \quad C_{\sigma,j} = \frac{1}{\sqrt{3}} e^{i2\pi(j-1)\sigma/3}. \quad (\text{A5})$$

and $\bar{A}_{j,s=\downarrow,\tau} = \mathcal{U} \mathcal{K} \bar{A}_{j,s=\uparrow,-\tau}$. Here, \mathcal{K} is complex conjugation and $\mathcal{U} = ie^{i\pi S_y}$ with S_x in the spin-3/2 representation. The complex phase is given by the in-plane momenta $e^{i\phi} = (p_x + ip_y)/p$, with $p = |\mathbf{p}|$ and the coefficients $a_{S_z}(p)$ are found numerically via exact diagonalisation of the Luttinger Hamiltonian (1), shown in Fig. 9. Finally, we have introduced two orthogonal vectors $\hat{e}, \hat{\delta}$, which account for the even and odd parity (inversion in z -axis) of the wave function/spin components, $a_{S_z}(p, z)$.

For completeness we also specify the symmetry properties of the wavefunctions. The symmetries of a honeycomb system are $2\pi/3$ and π rotations, reflections, and time reversal. At the high symmetry points $\mathbf{p} = \mathbf{0}$, using the explicit form of the wavefunctions (A4) and (A5)

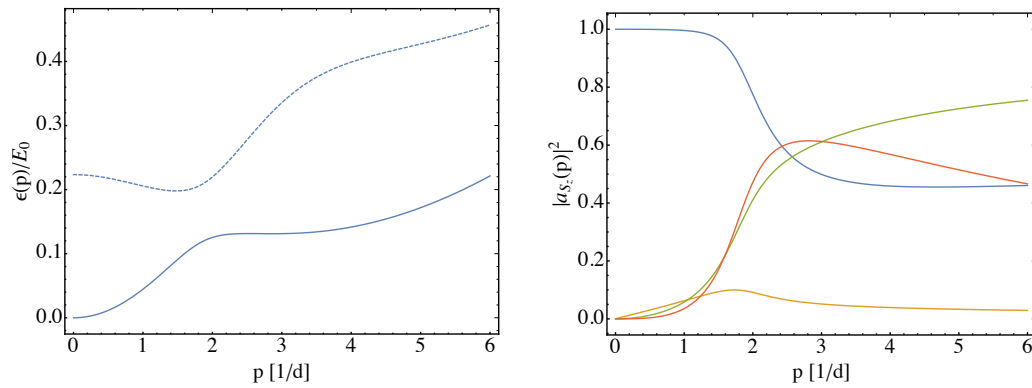


FIG. 9: (a) 2DHG spectrum, $\epsilon(p)/E_0$ for InAs. Solid blue line corresponds to the doubly degenerate spectrum that enters the computations of the effective Dirac Hamiltonian (4), the dashed line is the next highest subband, which is ignored in our approximations. (b) Probability densities $|a_{S_z}(p)|^2$ of each physical spin component S_z , presented in (A5).

1185 the transformations are found to be

$$\begin{aligned}
 D(C_{3z}) |s, \tau, \sigma\rangle &= -e^{2i\pi\sigma/3} |s, \tau, \sigma\rangle \\
 D(C_{2z}) |s, \tau, \sigma\rangle &= -is |s, -\tau, \sigma\rangle \\
 D(C_{2x}) |s, \tau, \sigma\rangle &= i |s, \tau, -\sigma\rangle \\
 D(C_{2y}) |s, \tau, \sigma\rangle &= -s |s, -\tau, -\sigma\rangle \\
 D(\mathcal{T}) |s, \tau, \sigma\rangle &= -s |s, -\tau, -\sigma\rangle.
 \end{aligned}
 \tag{A6}$$

1186 The resulting transformation properties are summarized in Table II.

Appendix B: Polarization Operators

1187

1188

1. Preliminaries

1189 The polarisation operators are given by (setting velocity $v = 1$ for ease of notation)

$$i\Pi_{\mu\nu}(p_0, \mathbf{p}) = \int \frac{dq_0 d^2q}{(2\pi)^3} \frac{\text{Tr} [J^\mu h^\alpha J^\nu h^\beta]}{\tilde{q}_0^2 - \mathbf{q}^2 - \eta^2} \frac{\tilde{q}_\beta(\tilde{q} + \tilde{p})_\alpha}{(\tilde{q}_0 + p_0)^2 - (\mathbf{q} + \mathbf{p})^2 - \eta^2}$$

1190 with modified momenta $\tilde{q}_\alpha \in \{q_0 + \mu, \mathbf{q}, \eta\}$, $\tilde{p}_\alpha \in \{p_0 + \mu, \mathbf{q}, 0\}$, and vertices: $h^\alpha \in \{\mathbb{1}, \sigma_x, \tau_z \sigma_y, s_z \tau_z \sigma_z\}$, pertaining to the Hamiltonian,
1191 and $J_I^\mu \in \{\mathbb{1}, \sigma_\pm, \tau_z \sigma_z, \tau_z s_z, \tau_z s_z \sigma_\pm, \sigma_z s_z\}$, $J_{II}^\mu \in \{\mathbb{1}, \sigma_\pm, \sigma_z s_z\} \otimes \tau_\pm$, pertaining to the interactions.

1192 By evaluating the frequency integral by residues, the expression reduces to

$$\begin{aligned} i\Pi_{\mu\nu}(p) &= \int \frac{d^2q}{(2\pi)^3} \frac{\text{Tr} [J^\mu h^\alpha J^\nu h^\beta]}{q_0^2 - \mathbf{q}^2 - \eta^2} \frac{q_\beta(q + p)_\alpha}{(q_0 + p_0)^2 - (\mathbf{q} + \mathbf{p})^2 - \eta^2} [1 - (\Theta(\mu - \varepsilon_q) + \Theta(\mu - \varepsilon_{\mathbf{q}+\mathbf{p}}))] \\ &\equiv i\Pi_{\mu\nu}^{(0)}(p) + i\delta\Pi_{\mu\nu}(p) \end{aligned} \quad (\text{B1})$$

1193 where $\Pi_{\mu\nu}^{(0)}(p)$ is defined as the polarization operator at zero chemical potential $\mu = 0$, i.e. the interband polarization operator [30]. The
1194 remaining contribution $\delta\Pi_{\mu\nu}(p)$ is referred to as the intraband polarization operator.

1195 This function is divergent and requires regularization; we use dimensional regularization, and after some manipulations, we arrive at

$$i\Pi_{\mu\nu}^{(0)}(p) = \int_0^1 dy \int \frac{d^3l}{(2\pi)^3} \frac{\text{Tr} [J^\mu h^\alpha J^\nu h^\beta] (l - yp)_\beta (l + (1 - y)p)_\alpha}{[l^2 - \Delta(p_0, \mathbf{p}, y)]^2} \quad (\text{B2})$$

1196 with $\Delta(p_0, \mathbf{p}, y) = \eta^2 - y(1 - y)(p_0^2 - \mathbf{p}^2)$. The expression (B2) is evaluated analytically, at zero frequency $p_0 = 0$, and for all μ, ν ; the
1197 results are printed in Appendix B2. The second contribution $\delta\Pi_{\mu\nu}(p)$, which depends on chemical potential μ , can be evaluated through
1198 the rearrangements,

$$\begin{aligned} \delta\Pi_{\mu\nu}(p) &= \int \frac{d^2q}{(2\pi)^2} \frac{\text{Tr} [J^\mu h^\alpha J^\nu h^\beta] q_\beta(q + p)_\alpha \Theta(\mu - \varepsilon_q)}{2\varepsilon_q [(\varepsilon_q + p_0)^2 - (\mathbf{q} + \mathbf{p})^2 - \eta^2]} + \frac{\text{Tr} [J^\mu h^\alpha J^\nu h^\beta] q_\beta(q + p)_\alpha \Theta(\mu - \varepsilon_{\mathbf{q}+\mathbf{p}})}{2\varepsilon_{\mathbf{q}+\mathbf{p}} [(\varepsilon_{\mathbf{q}+\mathbf{p}} - p_0)^2 - q^2 - \eta^2]} \\ &= - \sum_{\sigma=\pm} \sigma \int \frac{dq d\theta}{(2\pi)^2} \frac{\text{Tr} [J^\mu h^\alpha J^\nu h^\beta] q_\beta(q + \sigma p)_\alpha \Theta(\mu - \varepsilon_q)}{\cos \theta + a_\sigma} \frac{1}{4\varepsilon_q p}, \end{aligned} \quad (\text{B3})$$

1199 where,

$$a_\sigma = \frac{q^2 + p^2 + \eta^2 - (\varepsilon_q + \sigma p_0 e^{i\theta})^2}{2qp\sigma}, \quad a_\sigma^0 \equiv a_\sigma(p_0 = 0) = \sigma \frac{p}{2q}$$

1200 We specialise to the static limit $p_0 = 0$, which means we only need to keep the principle value of $1/(a_\sigma + \cos \theta)$.

1201

2. Results

1202 We decomposed the polarization operator into interband and intraband contributions,

$$\Pi_{\mu s \tau}(p_0, \mathbf{p}) = \Pi_{\mu s \tau}^0(p_0, \mathbf{p}) + \delta\Pi_{\mu s \tau}(p_0, \mathbf{p}). \quad (\text{B4})$$

1203 indices $\mu = 0, x, y, z, s = 0, s_z, \tau = 0, \tau_z$. We denote the relatively few distinct non-zero polarization operators as

$$\begin{aligned} \Pi_\pm(\mathbf{p}) &= \Pi_{z00,x00}(0, \mathbf{p}) \pm i\Pi_{z00,y00}(0, \mathbf{p}) = \Pi_{zs\tau,xs\tau}(0, \mathbf{p}) \pm i\Pi_{zs\tau,ys\tau}(0, \mathbf{p}), \\ \Pi_0(\mathbf{p}) &= \Pi_{0s\tau,0s\tau}(0, \mathbf{p}), \\ \Pi_z &= \Pi_{zs\tau,zs\tau}(0, \mathbf{p}), \\ \Pi_\eta &= \Pi_{zs_z 0; 0s_z \tau}(\mathbf{p}) = \Pi_{z0\tau_z; 000}(\mathbf{p}) \end{aligned} \quad (\text{B5})$$

1204 Here we factor out $N = 8$ coming from the trace (spin \times pseudospin \times valley). Subscripts x, y, z correspond to pseudospin, while s, τ
1205 correspond to spin s_z and valley τ_z . We then calculate the following expressions,

$$\begin{aligned}
i\Pi_{0s;0s}^{(0)}(\mathbf{p}) &= N \int_0^1 dy \int \frac{d^d l}{(2\pi)^d} \frac{l_0^2 + l_x^2 + l_y^2 - y(1-y)\mathbf{p}^2 + \eta^2}{[l^2 - \Delta(p_0, \mathbf{p}, y)]^2} \\
&= N \int_0^1 dy \left[\frac{1}{2} \frac{i\Gamma(1-d/2)}{(4\pi)^{d/2}\Gamma(2)} \Delta^{d/2-1} + (\eta^2 - y(1-y)\mathbf{p}^2) \frac{i\Gamma(2-d/2)}{(4\pi)^{d/2}\Gamma(2)} \Delta^{d/2-2} \right] \\
&= N \frac{i}{8\pi} \int_0^1 dy \left[-(\eta^2 + y(1-y)\mathbf{p}^2)^{1/2} + (\eta^2 - y(1-y)\mathbf{p}^2) (\eta^2 + y(1-y)\mathbf{p}^2)^{-1/2} \right] \\
&= N \frac{i}{8\pi} \int_0^1 dy \left[-2y(1-y)\mathbf{p}^2 (\eta^2 + y(1-y)\mathbf{p}^2)^{-1/2} \right] \\
&= N \frac{i}{8\pi} \left[-\eta + \frac{1}{2p} (4\eta^2 - p^2) \arcsin \left[\frac{p}{\sqrt{4\eta^2 + p^2}} \right] \right]
\end{aligned} \tag{B6}$$

1206 All other computations follow similarly,

$$\begin{aligned}
i\Pi_{zs;zs}^{(0)}(\mathbf{p}) &= N \frac{i}{8\pi} \left[2\eta + \frac{1}{p} (4\eta^2 + p^2) \arcsin \left[\frac{p}{\sqrt{4\eta^2 + p^2}} \right] \right], \\
i\Pi_{xs;xs}^{(0)}(\mathbf{p}) &= N \frac{i}{8\pi} \frac{p_y^2}{p^2} \left[\eta - \frac{1}{2p} (4\eta^2 - p^2) \arcsin \left[\frac{p}{\sqrt{4\eta^2 + p^2}} \right] \right], \\
i\Pi_{ys;ys}^{(0)}(\mathbf{p}) &= N \frac{i}{8\pi} \frac{p_x^2}{p^2} \left[\eta - \frac{1}{2p} (4\eta^2 - p^2) \arcsin \left[\frac{p}{\sqrt{4\eta^2 + p^2}} \right] \right], \\
i\Pi_{xs;ys}^{(0)}(\mathbf{p}) &= i\Pi_{ys;xs}^{(0)}(\mathbf{p}) = N \frac{i}{8\pi} \frac{p_x p_y}{p^2} \left[-\eta + \frac{1}{2p} (4\eta^2 - p^2) \arcsin \left[\frac{p}{\sqrt{4\eta^2 + p^2}} \right] \right], \\
i\Pi_{x00;0s_z\tau_z}^{(0)}(\mathbf{p}) &= -i\Pi_{0s_z\tau_z;x00}^{(0)}(\mathbf{p}) = i\Pi_{xs\tau;000}^{(0)}(\mathbf{p}) = -i\Pi_{000;xs\tau}^{(0)}(\mathbf{p}) \\
&= -\frac{iN}{8\pi} \frac{ip_y}{p} \left[2\eta \arcsin \left[\frac{p}{\sqrt{4\eta^2 + p^2}} \right] \right], \\
i\Pi_{y00;0s_z\tau_z}^{(0)}(\mathbf{p}) &= -i\Pi_{0s_z\tau_z;y\bar{s}}^{(0)}(\mathbf{p}) = i\Pi_{ys\tau;000}^{(0)}(\mathbf{p}) = -i\Pi_{000;ys\tau}^{(0)}(\mathbf{p}) \\
&= \frac{iN}{8\pi} \frac{ip_x}{p} \left[2\eta \arcsin \left[\frac{p}{\sqrt{4\eta^2 + p^2}} \right] \right]
\end{aligned} \tag{B7}$$

1207 We now consider the contribution explicitly dependent upon the chemical potential. Again with $p_0 = 0$, one finds

$$\begin{aligned}
\delta\Pi_{0s;0s}(\mathbf{p}) &= \frac{N}{8\pi} \left[-2\mu + \eta - \frac{1}{2p}(4\eta^2 - p^2) \arcsin\left(\frac{p}{\sqrt{4\eta^2 + p^2}}\right) \right] \\
\delta\Pi_{x;x}(\mathbf{p}) &= \frac{N}{8\pi} \frac{p_y^2}{p^2} \left[-\eta + \frac{1}{2p}(4\eta^2 - p^2) \arcsin\left(\frac{p}{\sqrt{4\eta^2 + p^2}}\right) \right] \\
\delta\Pi_{y;y}(\mathbf{p}) &= \frac{N}{8\pi} \frac{p_x^2}{p^2} \left[-\eta + \frac{1}{2p}(4\eta^2 - p^2) \arcsin\left(\frac{p}{\sqrt{4\eta^2 + p^2}}\right) \right] \\
\delta\Pi_{z;z}(\mathbf{p}) &= \frac{N}{8\pi} \left[2\mu - 2\eta - \frac{1}{p}(4\eta^2 + p^2) \arcsin\left(\frac{p}{\sqrt{4\eta^2 + p^2}}\right) \right] \\
\delta\Pi_{x;y}(\mathbf{p}) &= \frac{N}{8\pi} \frac{p_x p_y}{p^2} \left[\eta - \frac{1}{2p}(4\eta^2 - p^2) \arcsin\left(\frac{p}{\sqrt{4\eta^2 + p^2}}\right) \right] \\
\delta\Pi_{x;z}(\mathbf{p}) &= -\frac{N}{8\pi} i p_y \\
\delta\Pi_{y;z}(\mathbf{p}) &= \frac{N}{8\pi} i p_x \\
\delta\Pi_{x00;0\tau}(\mathbf{p}) &= \frac{N}{8\pi} \frac{i2\eta p_y}{p} \arcsin\left(\frac{\sqrt{p^2}}{\sqrt{4\eta^2 + p^2}}\right) \\
\delta\Pi_{xs\tau;000}(\mathbf{p}) &= \frac{N}{8\pi} \frac{i2\eta p_y}{p} \arcsin\left(\frac{\sqrt{p^2}}{\sqrt{4\eta^2 + p^2}}\right) \\
\delta\Pi_{y00;0s\tau}(\mathbf{p}) &= -\frac{N}{8\pi} \frac{i2\eta p_x}{p} \arcsin\left(\frac{\sqrt{p^2}}{\sqrt{4\eta^2 + p^2}}\right) \\
\delta\Pi_{ys\tau;000}(\mathbf{p}) &= -\frac{N}{8\pi} \frac{i2\eta p_x}{p} \arcsin\left(\frac{\sqrt{p^2}}{\sqrt{4\eta^2 + p^2}}\right) \\
\delta\Pi_{zs_s;0s\tau}(\mathbf{p}) &= \delta\Pi_{z0\tau_z;000}(\mathbf{p}) = \frac{N}{8\pi} 2\eta
\end{aligned} \tag{B8}$$

1208 Now (with $s = 0, s_z$), we relate to channel I (here ordering of $\tau\bar{\tau}$ does not affect the result):

$$\begin{aligned}
\Pi_{0;0}^{\tau\bar{\tau}}(\mathbf{p}) &= \frac{1}{2} \Pi_{z;z}(\mathbf{p}) \\
\Pi_{x;x}^{\tau\bar{\tau}}(\mathbf{p}) &= \frac{1}{2} \Pi_{y;y}(\mathbf{p}) \\
\Pi_{y;y}^{\tau\bar{\tau}}(\mathbf{p}) &= \frac{1}{2} \Pi_{x;x}(\mathbf{p}) \\
\Pi_{z;z}^{\tau\bar{\tau}}(\mathbf{p}) &= \frac{1}{2} \Pi_{0;0}(\mathbf{p}) \\
\Pi_{x;y}^{\tau\bar{\tau}}(\mathbf{p}) &= -\frac{1}{2} \Pi_{x;y}(\mathbf{p}) \\
\Pi_{x;0}^{\tau\bar{\tau}}(\mathbf{p}) &= 0 \\
\Pi_{y;0}^{\tau\bar{\tau}}(\mathbf{p}) &= 0 \\
\Pi_{z;0}^{\tau\bar{\tau}}(\mathbf{p}) &= \frac{1}{2} \Pi_{zs;0}(\mathbf{p}) = N \frac{\eta}{8\pi} \\
\Pi_{x;z}^{\tau\bar{\tau}}(\mathbf{p}) &= 0 \\
\Pi_{y;z}^{\tau\bar{\tau}}(\mathbf{p}) &= 0.
\end{aligned} \tag{B9}$$

1209

Appendix C: Interactions in Cooper channel

1210 To obtain the interactions in band basis, we define the creation operator $\tilde{\psi}_k^\dagger$ which creates a fermion in the upper band, while ψ_k^\dagger creates
1211 a fermion of definite pseudospin. Changing to the band basis, we use

$$\begin{aligned} \psi_k &= \mathcal{U}_{k,\tau,s} \tilde{\psi}_k \\ \mathcal{U}_{k,\tau,s} &= \begin{pmatrix} w_{\tau,s}^a(k) & w_{\tau,s}^a(k) \\ w_{\tau,s}^b(k)e^{i\tau\theta_k} & w_{\tau,s}^b(k)e^{i\tau\theta_k} \end{pmatrix} \end{aligned} \quad (\text{C1})$$

1212 with the wavefunction components given by, $w_{\tau,s}^a(k) \equiv vk/\sqrt{2\epsilon_k(\epsilon_k - \alpha\tau\eta)}$, $w_{\tau,s}^b(k) \equiv (\tau\epsilon_k - \alpha\eta)/(vk)w_{\alpha,k,\tau}^a$, with functions
1213 $w_{\tau,s}^a(k), w_{\tau,s}^b(k)$ similarly defined for the lower band eigenstates, but not needed.

1214 We then keep only the upper band, e.g. we use the projections

$$\begin{aligned} \mathcal{U}_{[1]}^\dagger \sigma_x \mathcal{U}_{[2]} \Big|_{++} &= \left(w_{[1]}^a w_{[2]}^b e^{i\tau_2\theta_{k_2}} + w_{[2]}^a w_{[1]}^b e^{-i\tau_1\theta_{k_1}} \right), \\ \mathcal{U}_{[1]}^\dagger \sigma_y \mathcal{U}_{[2]} \Big|_{++} &= i \left(-w_{[1]}^a w_{[2]}^b e^{i\tau_2\theta_{k_2}} + w_{[2]}^a w_{[1]}^b e^{-i\tau_1\theta_{k_1}} \right), \\ \mathcal{U}_{[1]}^\dagger \sigma_z \mathcal{U}_{[2]} \Big|_{++} &= \left(w_{[1]}^a w_{[2]}^a - w_{[1]}^b w_{[2]}^b e^{-i\tau_1\theta_{k_1} + i\tau_2\theta_{k_2}} \right), \\ \mathcal{U}_{[1]}^\dagger \sigma_0 \mathcal{U}_{[2]} \Big|_{++} &= \left(w_{[1]}^a w_{[2]}^a + w_{[1]}^b w_{[2]}^b e^{-i\tau_1\theta_{k_1} + i\tau_2\theta_{k_2}} \right). \end{aligned} \quad (\text{C2})$$

1215 We compress notation such that indices are $[1] = \{k_1, \tau_1, s_1\}$. The notation “ $|_{++}$ ” indicates that we consider just the upper-band
1216 contribution. The phase factors owe to the single particle Berry phase and play a central role in the pairing mechanism.

1217 In the Cooper channel, $\mathbf{k}_1 = -\mathbf{k}_3$, $\mathbf{k}_2 = -\mathbf{k}_4$, such that $\theta_{k_3} = \pi + \theta_{k_1}$, $\theta_{k_4} = \pi + \theta_{k_2}$. The matrix elements of the screened Coulomb
1218 interaction in the upper band, separated into intravalley and intervalley Cooper channels, are obtained as,

$$\begin{aligned} \mathcal{V}_{intra} &= \sum_{\tau_i, s_i, \mathbf{k}_i} \left(\mathcal{U}_{[1]}^\dagger \otimes \mathcal{U}_{[3]}^\dagger \hat{V}_I \mathcal{U}_{[2]} \otimes \mathcal{U}_{[4]} \right) \Big|_{++} \delta_{\tau_1, \tau_2, \tau_3, \tau_4} \delta_{s_1, s_2} \delta_{s_3, s_4} \delta_{\mathbf{k}_1, -\mathbf{k}_3} \delta_{\mathbf{k}_2, -\mathbf{k}_4}, \\ \mathcal{V}_{inter} &= \sum_{\tau_i, s_i, \mathbf{k}_i} \left\{ \left(\mathcal{U}_{[1]}^\dagger \otimes \mathcal{U}_{[3]}^\dagger \hat{V}_I \mathcal{U}_{[2]} \otimes \mathcal{U}_{[4]} \right) \Big|_{++} \delta_{\tau_1, \tau_2, -\tau_3, -\tau_4} \delta_{s_1, s_2} \delta_{s_3, s_4} \delta_{\mathbf{k}_1, -\mathbf{k}_3} \delta_{\mathbf{k}_2, -\mathbf{k}_4} \right. \\ &\quad \left. + \left(\mathcal{U}_{[1]}^\dagger \otimes \mathcal{U}_{[3]}^\dagger \hat{V}_{II} \mathcal{U}_{[2]} \otimes \mathcal{U}_{[4]} \right) \Big|_{++} \delta_{\tau_1, -\tau_2, -\tau_3, \tau_4} \delta_{s_1, s_3} \delta_{s_2, s_4} \delta_{\mathbf{k}_1, -\mathbf{k}_3} \delta_{\mathbf{k}_2, -\mathbf{k}_4} \right\}. \end{aligned} \quad (\text{C3})$$

1219 We compactly write this as a spin and valley tensor (pseudospin has been removed since we work in band basis and keep just the upper
1220 band), using the scattering angle $\theta \equiv \theta_{\mathbf{k}_2} - \theta_{\mathbf{k}_1}$, $\hat{\mathcal{V}}(\theta) = g_{abcd}(\theta) s_a s_b \tau_c \tau_d + j_{ab\alpha\beta}(\theta) s_a s_b \tau_\alpha \tau_\beta$, where $a, b, c, d \in \{0, z\}$ and $\alpha, \beta \in \pm$. We
1221 explicitly display the angular dependence of the interaction matrix elements. Considering the angular momentum channel, l ,

$$\begin{aligned} \hat{\mathcal{V}}_l &= \int \frac{d\theta}{2\pi} e^{il\theta} [g_{abcd} s_a s_b \tau_c \tau_d + j_{ab\alpha\beta} s_a s_b \tau_\alpha \tau_\beta] \\ &= g_{abcd}^l s_a s_b \tau_c \tau_d + j_{ab\alpha\beta}^l s_a s_b \tau_\alpha \tau_\beta \end{aligned} \quad (\text{C4})$$

1222 We find that $l = \pm 1$ (p -wave) and $l = 0$ (s -wave) are the dominant channels. The resulting tensor is given in equations (12) and (13) in
1223 the main text.

1224

Appendix D: Effective tight-binding model for the superlattice

1225 In order to derive the effective lattice model, we introduce a basis of Wannier orbitals $|\mathbf{R}, \alpha\rangle$ localised at the sites \mathbf{R} of the honeycomb
1226 lattice, with α being a spin index defined by the action of threefold rotations (C_{3z})

$$u(C_{3z})|\mathbf{R}, \alpha\rangle = e^{\frac{2\pi i}{3}\alpha}|\Lambda\mathbf{R}, \alpha\rangle, \quad (\text{D1})$$

1227 where $\alpha = \{\pm\frac{3}{2}, \pm\frac{1}{2}\}$. We consider only the four lowest-energy orbitals on each site.

1228 The lattice Hamiltonian has the form

$$H = \sum T_{\alpha, \alpha'}(\mathbf{R}, \mathbf{R}') c_{\mathbf{R}, \alpha}^\dagger c_{\mathbf{R}', \alpha'} \quad (\text{D2})$$

1229 where

$$T_{\alpha, \alpha'}(\mathbf{R}, \mathbf{R}') = \langle \mathbf{R}, \alpha | H_{2DHG} | \mathbf{R}', \alpha' \rangle, \quad (\text{D3})$$

1230 with H_{2DHG} defined in (1). There is a splitting between the on-site energies $T_{\alpha\alpha}(\mathbf{R}, \mathbf{R}) = \varepsilon_\alpha = \varepsilon_{|\alpha|}$ for the $\alpha = \pm\frac{3}{2}$ and $\alpha = \pm\frac{1}{2}$ states, and
1231 we consider an effective model involving only the $\alpha = \pm\frac{3}{2}$ states, which are lowest in energy, and denote $\alpha = \frac{3}{2}s$ where s is the spin index
1232 used throughout the main text, and $c_{\mathbf{R}, \alpha} \rightarrow c_{\mathbf{R}, s}$.

1233 The topological mass term originates from nearest neighbour hopping terms which involve a spin transition $\alpha' - \alpha = \pm 2$. By symmetry
1234 we find, for hopping from a site \mathbf{R} to a nearest neighbour $\mathbf{R} + \mathbf{d}$,

$$T_{\mp\frac{1}{2}, \pm\frac{3}{2}}(\mathbf{R} + \mathbf{d}, \mathbf{R}) = \lambda d_\pm^2. \quad (\text{D4})$$

1235 An effective spin-conserving next nearest neighbour hopping term arises due to two consecutive hoppings with initial, intermediate and final
1236 sites $\mathbf{R}, \mathbf{R} + \mathbf{d}$, and $\mathbf{R} + \mathbf{d} + \mathbf{d}'$ respectively

$$T_{ss}^{\text{eff}}(\mathbf{R} + \mathbf{d} + \mathbf{d}', \mathbf{R}) = \frac{\lambda^2}{\varepsilon_{\frac{3}{2}} - \varepsilon_{\frac{1}{2}}} |\mathbf{d}|^2 e^{2is\sigma(\theta' - \theta)} \quad (\text{D5})$$

1237 where θ, θ' are the hopping directions in the first and second steps respectively and $\sigma = +1, -1$ when $\mathbf{R} \in A, B$ respectively.

1238 Choosing lattice vectors $\mathbf{a}_1 = (a, 0)$, $\mathbf{a}_2 = (a/2, a\sqrt{3}/2)$, and denoting the three nearest neighbour bonds $\mathbf{d}_i = \mathbf{R} - \mathbf{R}'$ with \mathbf{R}' in the
1239 A sublattice and \mathbf{R} a neighbouring site, and the six next nearest neighbour bonds $\tilde{\mathbf{d}}_n$ which are vectors of length a directed along angles
1240 $\theta_n = \frac{n\pi}{3}$ for $n = \{0, 1, 2, 3, 4, 5\}$, we obtain an effective Hamiltonian involving only the $|\alpha| = \frac{3}{2}$ states (after absorbing the on-site potential
1241 into the chemical potential)

$$H = -t \sum_{\langle \mathbf{R} + \mathbf{d}_i, \mathbf{R} \rangle} c_{\mathbf{R} + \mathbf{d}_i, s}^\dagger c_{\mathbf{R}, s} - t' \sum_{\langle \mathbf{R} + \tilde{\mathbf{d}}_n, \mathbf{R} \rangle} e^{is\sigma\varphi_n} c_{\mathbf{R} + \tilde{\mathbf{d}}_n, s}^\dagger c_{\mathbf{R}, s} \quad (\text{D6})$$

1242 where $\varphi_n = \frac{2\pi}{3}$ for $n = 0, 2, 4$ and $\varphi_n = -\frac{2\pi}{3}$ for $n = 1, 3, 5$.

1243 We make contact between the two forms of the normal state Hamiltonian by expanding the Hamiltonian near the K points, and reproduce
1244 the effective Dirac Hamiltonian

$$\mathcal{H}(\tau\mathbf{K} + \mathbf{k}) \approx v(\tau k_x \sigma_x + k_y \sigma_y) + \eta \tau \sigma_z s_z \quad (\text{D7})$$

1245 where we find the relation between the parameters in the Dirac theory and in the real space model

$$v = \frac{\sqrt{3}at}{2}, \quad \eta = \frac{9}{2}t' \quad (\text{D8})$$

¹²⁴⁶ Near the K points we have the upper band eigenstates

$$\tilde{\psi}_{\mathbf{k}\tau s}^\dagger = \sum_{\mathbf{R}} \varphi_{\mathbf{k}\tau s}(\mathbf{R}) c_{\mathbf{R}s}^\dagger \quad (\text{D9})$$

¹²⁴⁷ with symmetry properties $\varphi_{\mathbf{k}\tau s}(-\mathbf{R}) = \varphi_{-\mathbf{k}\bar{\tau}s}(\mathbf{R})$ and $\varphi_{-\mathbf{k}\bar{\tau}\downarrow}(\mathbf{R}) = \varphi_{\mathbf{k}\tau\uparrow}^*(\mathbf{R})$. Explicitly,

$$\varphi_{\mathbf{k}\tau s}(\mathbf{R}) = \frac{1}{\sqrt{2}} e^{i(\tau\mathbf{K}+\mathbf{k})\cdot\mathbf{R}} (w_{\tau,s}^a(k)a(\mathbf{R}) + e^{i\tau\theta_{\mathbf{k}}} w_{\tau,s}^a(k)b(\mathbf{R})) \quad (\text{D10})$$

¹²⁴⁸ with $a(\mathbf{R}) = \{1, 0\}$, $b(\mathbf{R}) = \{0, 1\}$, for $\mathbf{R} \in A, B$ respectively, and the functions $w_{\tau,s}^a(k)$ and $w_{\tau,s}^b(k)$ are defined in Section C. We shall use
¹²⁴⁹ these wavefunctions to obtain a real space form for the the superconducting gap functions we have written in momentum space in Section
¹²⁵⁰ V,

Appendix E: The pairing term in the lattice representation

1251

1252 The mean field BdG Hamiltonian is

$$H = \sum_{\mathbf{k}, \tau, s} \varepsilon_{\mathbf{k}} \tilde{\psi}_{\mathbf{k}\tau s}^\dagger \tilde{\psi}_{\mathbf{k}\tau s} + \frac{1}{2} \sum_{\mathbf{k}, -\mathbf{k}, \tau, \tau', s, s'} \tilde{\psi}_{\mathbf{k}\tau s}^\dagger (\Delta_{\mathbf{k}})_{\tau s, \tau' s'} \tilde{\psi}_{-\mathbf{k}\tau' s'}^\dagger + \text{h.c.} \quad (\text{E1})$$

1253 where we have used $\psi_{\mathbf{k}\tau s}$ to refer to the upper band creation operator, as in the previous subsection. The three superconducting phases we
1254 study are given by

$$\Delta_{\mathbf{k}} = \Delta_k \times \begin{cases} d_s^z s_z \tau_0 (\tau_y s_y) \\ e^{\pm i\theta_{\mathbf{k}}} d_s^z s_z \tau_z (\tau_y s_y) \\ e^{i\tau_z (\phi - \theta_{\mathbf{k}})} (d_s^x s_x + d_s^y s_y) \tau_y (\tau_y s_y) \end{cases} \quad (\text{E2})$$

1255 for the s_τ , $p + ip$ and $p + i\tau p$ phases respectively. We have added a factor Δ_k absent in the main text. This is a smooth function peaked at
1256 the Fermi momentum, encapsulating the fact that pairing should only occur near the Fermi surface, and should be retained in deriving the
1257 correct real space gap function. Writing

$$\Delta_{\mathbf{k}; \tau\tau'; ss'} = \Delta_{\tau\tau'}(\mathbf{k}) (d^\mu s_\mu i\hat{s}_y)_{ss'} \quad , \quad (\text{E3})$$

1258 to separate out the spin structure, we can use the upper band wavefunctions to go to the coordinate representation in terms of the full real
1259 space creation operator $c_{\mathbf{r}s}^\dagger$,

$$H = \frac{1}{2} \sum (d^\mu s_\mu i\hat{s}_y)_{ss'} \varphi_{\mathbf{k}\tau s}(\mathbf{R}) \Delta_{\tau\tau'}(\mathbf{k}) \varphi_{-\mathbf{k}\tau' s'}(\mathbf{R}') c_{\mathbf{R}s}^\dagger c_{\mathbf{R}'s'}^\dagger = \frac{1}{2} \sum \Delta_{ss'}(\mathbf{R}, \mathbf{R}') c_{\mathbf{R}s}^\dagger c_{\mathbf{R}'s'}^\dagger \quad (\text{E4})$$

1260 Note that under inversion, $\mathbf{R} \rightarrow -\mathbf{R}$, $\mathbf{R}' \rightarrow -\mathbf{R}'$ we have

$$\begin{aligned} \Delta_{ss'}(-\mathbf{R}, -\mathbf{R}') &= \sum_{\mathbf{k}} (d^\mu \hat{s}_\mu i\hat{s}_y)_{ss'} \varphi_{-\mathbf{k}\bar{\tau}s}(\mathbf{R}) \Delta_{\tau\tau'}(\mathbf{k}) \varphi_{\mathbf{k}\bar{\tau}'s'}(\mathbf{R}') \\ &= \sum_{\mathbf{k}} (d^\mu \hat{s}_\mu i\hat{s}_y)_{ss'} \varphi_{\mathbf{k}\tau s}(\mathbf{R}) \Delta_{\bar{\tau}\bar{\tau}'}(-\mathbf{k}) \varphi_{-\mathbf{k}\tau' s}(\mathbf{R}) \end{aligned} \quad (\text{E5})$$

1261 and the valley structures are explicitly given by

$$\Delta_{\tau\tau'}(\mathbf{k}) = \Delta_k \times \begin{cases} (i\hat{\tau}_y)_{\tau\tau'} \\ e^{\pm i\theta_{\mathbf{k}}} (\hat{\tau}_z i\hat{\tau}_y)_{\tau\tau'} \\ e^{i\hat{\tau}_z (\phi - \theta_{\mathbf{k}})} \end{cases} \quad (\text{E6})$$

1262 We can now explicitly evaluate the functions $\Delta(\mathbf{R}, \mathbf{R}')$. We begin with the intervalley phases, which take the form

$$H_\Delta = \sum_{\mathbf{k}; s} \Delta_k e^{i\ell\theta_{\mathbf{k}}} \tilde{\psi}_{\mathbf{k}+s}^\dagger \tilde{\psi}_{-\mathbf{k}-\bar{s}}^\dagger \quad (\text{E7})$$

1263 where $\ell = 0$ for the s_\pm phase and $\ell = \pm 1$ for the $p \pm ip$ phases. Expanding $\tilde{\psi}_{\mathbf{k}\tau s}^\dagger$ in the position basis (D9) we find

$$H_\Delta = \sum \Delta_k e^{i\ell\theta_{\mathbf{k}}} \varphi_{\mathbf{k}+s}(\mathbf{R}) \varphi_{-\mathbf{k}-\bar{s}}(\mathbf{R}') c_{\mathbf{R}s}^\dagger c_{\mathbf{R}'\bar{s}}^\dagger = \sum \Delta(\mathbf{R}, \mathbf{R}') c_{\mathbf{R}\uparrow}^\dagger c_{\mathbf{R}'\downarrow}^\dagger \quad (\text{E8})$$

1264 where we may write

$$\Delta(\mathbf{R}, \mathbf{R}') = \sum_{\mathbf{k}} \Delta_k e^{i\ell\theta_{\mathbf{k}}} [\varphi_{\mathbf{k}+\uparrow}(\mathbf{R}) \varphi_{\mathbf{k}+\uparrow}^*(\mathbf{R}') - \varphi_{\mathbf{k}+\uparrow}(-\mathbf{R}) \varphi_{\mathbf{k}+\uparrow}^*(-\mathbf{R}')] . \quad (\text{E9})$$

1265 In order to perform the summation over k we introduce the functions $f_m^{\sigma\sigma'}(l)$ defined by

$$f_m^{\sigma\sigma'}(l) = \int \Delta_k w_{++}^\sigma(k) w_{++}^{\sigma'}(k) J_m(kl) \frac{k dk}{2\pi} , \quad (\text{E10})$$

1266 with $m = 0, 1, 2, \dots$, and the relation

$$\sum w_{++}^\sigma(k) w_{++}^{\sigma'}(k) \Delta_k e^{i(\mathbf{k} \cdot (\mathbf{R} - \mathbf{R}') + \ell \theta_k)} = i^{|\ell|} e^{i\ell\theta} f_{|\ell|}^{\sigma\sigma'}(|\mathbf{R} - \mathbf{R}'|) , \quad (\text{E11})$$

1267 where $\theta = \theta_{\mathbf{R}} - \theta_{\mathbf{R}'}$.

1268 The function $f_0^{\sigma\sigma'}(l)$ is peaked at $l = 0$ and oscillates over length scales $\sim k_F^{-1}$ with decaying amplitude, while for $m > 0$ the functions
1269 $f_m^{\sigma\sigma'}(l)$ vanish at $l = 0$, increase to a global maximum at $l \approx k_F^{-1}$ and then decays for larger values of l .

1270 In terms of the functions $f_m^{\sigma\sigma}(l)$ the gap $\Delta(\mathbf{R}, \mathbf{R}')$ is given by

$$\begin{aligned} & \Delta(\mathbf{R}, \mathbf{R}') \\ &= \frac{1}{2} \times \begin{cases} i^{|\ell|} e^{i\ell\theta} \left(f_{|\ell|}^{\sigma\sigma}(|\mathbf{R} - \mathbf{R}'|) e^{i\mathbf{K} \cdot (\mathbf{R} - \mathbf{R}')} - (-1)^\ell f_{|\ell|}^{\bar{\sigma}\bar{\sigma}}(|\mathbf{R} - \mathbf{R}'|) e^{-i\mathbf{K} \cdot (\mathbf{R} - \mathbf{R}')} \right) , & \mathbf{R}, \mathbf{R}' \in \sigma \\ e^{i\ell\theta} \left(i^{|\ell-1|} e^{i(\mathbf{K} \cdot (\mathbf{R} - \mathbf{R}') - \theta)} f_{|\ell-1|}^{AB}(|\mathbf{R} - \mathbf{R}'|) + (-1)^\ell i^{|\ell+1|} e^{-i(\mathbf{K} \cdot (\mathbf{R} - \mathbf{R}') - \theta)} f_{|\ell+1|}^{AB}(|\mathbf{R} - \mathbf{R}'|) \right) , & \mathbf{R} \in A, \mathbf{R}' \in B \\ e^{i\ell\theta} \left(i^{|\ell+1|} e^{i(\mathbf{K} \cdot (\mathbf{R} - \mathbf{R}') + \theta)} f_{|\ell+1|}^{AB}(|\mathbf{R} - \mathbf{R}'|) + (-1)^\ell i^{|\ell-1|} e^{-i(\mathbf{K} \cdot (\mathbf{R} - \mathbf{R}') + \theta)} f_{|\ell-1|}^{AB}(|\mathbf{R} - \mathbf{R}'|) \right) , & \mathbf{R} \in B, \mathbf{R}' \in A \end{cases} \end{aligned} \quad (\text{E12})$$

1271 Note that for $\mathbf{R}, \mathbf{R}' \in \sigma$ we have

$$\Delta(\mathbf{R}, \mathbf{R}') = -\frac{1}{2} i^{|\ell|} e^{i\ell\theta} \left(f_{|\ell|}^{\bar{\sigma}\bar{\sigma}}(|\mathbf{R} - \mathbf{R}'|) e^{i\mathbf{K} \cdot (\mathbf{R} - \mathbf{R}')} - (-1)^\ell f_{|\ell|}^{\sigma\sigma}(|\mathbf{R} - \mathbf{R}'|) e^{-i\mathbf{K} \cdot (\mathbf{R} - \mathbf{R}')} \right) \quad (\text{E13})$$

1272 while for $\mathbf{R}' \in A, \mathbf{R} \in B$ we have

$$\Delta(\mathbf{R}, \mathbf{R}') = \frac{1}{2} \left(i^{|\ell+1|} e^{i(\mathbf{K} \cdot (\mathbf{R} - \mathbf{R}') + (\ell+1)\theta_{|\mathbf{R} - \mathbf{R}'|})} f_{|\ell+1|}^{AB}(|\mathbf{R} - \mathbf{R}'|) + (-1)^\ell i^{|\ell-1|} e^{i(-\mathbf{K} \cdot (\mathbf{R} - \mathbf{R}') + (\ell-1)\theta)} f_{|\ell-1|}^{AB}(|\mathbf{R} - \mathbf{R}'|) \right) \quad (\text{E14})$$

1273 For nearest neighbours, $\mathbf{R} - \mathbf{R}' = \mathbf{d}_i$, recall that we have $\mathbf{K} \cdot \mathbf{d}_i = \{0, -2\pi/3, 2\pi/3\}$ and $\theta_{\mathbf{R}} = \theta_i = \{\pi/2, \pi/2 + 2\pi/3, \pi/2 + 4\pi/3\}$, giving
1274 us $\mathbf{K} \cdot \mathbf{R} + \theta_{\mathbf{R}} = \frac{\pi}{2}$. Thus for $\mathbf{R}' \in A$ we have

$$\Delta(\mathbf{R}' + \mathbf{d}_i, \mathbf{R}') = \frac{1}{2} e^{i\ell\theta_i} \left(i^{|\ell+1|+1} f_{|\ell+1|}^{AB}\left(\frac{a}{\sqrt{3}}\right) + (-1)^\ell i^{|\ell-1|-1} f_{|\ell-1|}^{AB}\left(\frac{a}{\sqrt{3}}\right) \right) \quad (\text{E15})$$

1275 For next nearest neighbours, $\mathbf{R} - \mathbf{R}' = \tilde{\mathbf{d}}'_n$ we have

$$e^{i\mathbf{K} \cdot (\mathbf{R} - \mathbf{R}')} = \begin{cases} e^{-\frac{2\pi i}{3}} , & i = 1, 3, 5 \\ e^{\frac{2\pi i}{3}} , & i = 2, 4, 6 \end{cases} \quad (\text{E16})$$

1276 which gives us, for $\mathbf{R} - \mathbf{R}' = \tilde{\mathbf{d}}'_n$

$$\Delta(\mathbf{R}, \mathbf{R}') = \begin{cases} \frac{1}{2} i^{|\ell|} e^{i\ell\theta'_i} \left(f_{|\ell|}^{\sigma\sigma}(a) e^{-\frac{2\pi i}{3}} - (-1)^\ell f_{|\ell|}^{\bar{\sigma}\bar{\sigma}}(a) e^{\frac{2\pi i}{3}} \right) , & i = 1, 3, 5 \\ \frac{1}{2} i^{|\ell|} e^{i\ell\theta'_i} \left(f_{|\ell|}^{\sigma\sigma}(a) e^{\frac{2\pi i}{3}} - (-1)^\ell f_{|\ell|}^{\bar{\sigma}\bar{\sigma}}(a) e^{-\frac{2\pi i}{3}} \right) , & i = 2, 4, 6 \end{cases} \quad (\text{E17})$$

1277 with θ'_i being the angle between \mathbf{d}'_i and the x axis.

1278

$a. s_\tau$

1279 We obtain the gap in the s_τ phase by setting $\ell = 0$ in (E12). For neighbour pairing we find (E15)

$$\Delta(\mathbf{R}' + \mathbf{d}_i, \mathbf{R}') = \frac{1}{2} f_1^{AB}\left(\frac{a}{\sqrt{3}}\right) (-1 + 1) = 0 \quad (\text{E18})$$

1280 and therefore restrict the pairing to next nearest neighbours only. The gap depends on the function $f_0^{\sigma\sigma}(a)$. Writing $f_0^{AA}(a) = \alpha + \beta$,
 1281 $f_0^{BB}(a) = \alpha - \beta$ we have from (E16)

$$\begin{aligned} \Delta(\mathbf{R}, \mathbf{R}') &= \begin{cases} \frac{1}{2} \left((\alpha + \beta)e^{-\frac{2\pi i}{3}} - (\alpha - \beta)e^{\frac{2\pi i}{3}} \right) , & i = 1, 3, 5 \\ \frac{1}{2} \left((\alpha + \beta)e^{\frac{2\pi i}{3}} - (\alpha - \beta)e^{-\frac{2\pi i}{3}} \right) , & i = 2, 4, 6 \end{cases} \\ &= \begin{cases} -\frac{1}{2}(\beta + i\sqrt{3}\alpha) , & i = 1, 3, 5 \\ -\frac{1}{2}(\beta - i\sqrt{3}\alpha) , & i = 2, 4, 6 \end{cases} \end{aligned} \quad (\text{E19})$$

1282 In the limit of spin-orbit interaction we have $\beta \rightarrow 0$. For the numerical diagonalisation we choose a gap in which $\beta = 0$ (since the spin-orbit
 1283 interaction is weak) and $\alpha = i\Delta'$, so that $\Delta(\mathbf{R}, \mathbf{R}')$ is purely real.

1284 *b. $p + ip$*

1285 For exact diagonalisation we take only the nearest neighbour pairing terms. For $\mathbf{R}' \in A$, $\mathbf{R} = \mathbf{R}' + \mathbf{d}_i$, the gap is given by setting $\ell = +1$
 1286 in (E15),

$$\begin{aligned} \Delta(\mathbf{R}, \mathbf{R}') &= \frac{1}{2}e^{i\theta} [-if_2^{AB}(R) + if_0^{AB}(R)] \\ &= \Delta' e^{i\theta} \end{aligned} \quad (\text{E20})$$

1287 where $\theta = \theta_{\mathbf{R}} - \theta_{\mathbf{R}'}$.

1288 *c. $p + i\tau p$*

1289 We now consider the $p + i\tau p$ phase. Since the \mathbf{d}_s vector is pinned in-plane for this phase, pairing is between the same spin species, i.e.
 1290 the gap is proportional to s_z . This way, BdG Hamiltonian can be decomposed into spin blocks, the Majoranas corner states associated to
 1291 each of which are related by time-reversal symmetry.

1292 The derivation then proceeds through more or less the same manipulations as above (c.f. Appendix A4 of [1]). It is possible to decompose
 1293 the pairing term into two identical spin blocks,

$$H_{\Delta} = \frac{1}{2} \sum_{\mathbf{k}, \tau, s} \Delta_{\mathbf{k}} e^{i\tau\phi} e^{-i\tau\theta_{\mathbf{k}}} \tilde{\psi}_{\mathbf{k}, \tau, s}^{\dagger} \tilde{\psi}_{-\mathbf{k}, \tau, s}^{\dagger} = \frac{1}{2} \sum_s \Delta(\mathbf{R}, \mathbf{R}') c_{\mathbf{R}, s}^{\dagger} c_{\mathbf{R}', s}^{\dagger} . \quad (\text{E21})$$

1294 Expanding $\tilde{\psi}_{\mathbf{k}, \tau, s}$ in the position basis (D9) we find

$$\begin{aligned} \Delta(\mathbf{R}, \mathbf{R}') &= \sum_{\mathbf{k}} \Delta_{\mathbf{k}} \left\{ \frac{1}{2} e^{i\{\mathbf{K} \cdot (\mathbf{R} + \mathbf{R}') + \mathbf{k} \cdot (\mathbf{R} - \mathbf{R}') + \phi - \theta_{\mathbf{k}}\}} [(w_{+,s}^a(\mathbf{k})a(\mathbf{R}) + e^{i\theta_{\mathbf{k}}} w_{+,s}^b(\mathbf{k})b(\mathbf{R})) (w_{+,s}^a(\mathbf{k})a(\mathbf{R}') - e^{i\theta_{\mathbf{k}}} w_{+,s}^b(\mathbf{k})b(\mathbf{R}'))] \right. \\ &\quad \left. + \frac{1}{2} e^{i\{-\mathbf{K} \cdot (\mathbf{R} + \mathbf{R}') + \mathbf{k} \cdot (\mathbf{R} - \mathbf{R}') - \phi + \theta_{\mathbf{k}}\}} [(w_{-,s}^a(\mathbf{k})a(\mathbf{R}) + e^{-i\theta_{\mathbf{k}}} w_{-,s}^b(\mathbf{k})b(\mathbf{R})) (w_{-,s}^a(\mathbf{k})a(\mathbf{R}') - e^{-i\theta_{\mathbf{k}}} w_{-,s}^b(\mathbf{k})b(\mathbf{R}'))] \right\} . \end{aligned} \quad (\text{E22})$$

1295 Performing the summation over \mathbf{k} yields functions $f_m^{\sigma\sigma'}(|\mathbf{R} - \mathbf{R}'|)$ which all vanish at small separations $\mathbf{R} - \mathbf{R}' \ll k_F^{-1}$ except for $m = 0$.
 1296 For purposes of exact diagonalisation, we keep only terms involving nearest neighbours, which correspond to those that cancel the winding
 1297 factor $e^{i\theta_{\mathbf{k}}}$. This gives

$$\begin{aligned} \Delta(\mathbf{R}, \mathbf{R}') &= \sum_{\mathbf{k}} \Delta_{\mathbf{k}} \left\{ \frac{1}{2} e^{i\{\mathbf{K} \cdot (\mathbf{R} + \mathbf{R}') + \mathbf{k} \cdot (\mathbf{R} - \mathbf{R}') + \phi - \theta_{\mathbf{k}}\}} w_{+,s}^a w_{+,s}^b e^{i\theta_{\mathbf{k}}} (-a(\mathbf{R})b(\mathbf{R}') + b(\mathbf{R})a(\mathbf{R}')) \right. \\ &\quad \left. + \frac{1}{2} e^{i\{-\mathbf{K} \cdot (\mathbf{R} + \mathbf{R}') + \mathbf{k} \cdot (\mathbf{R} - \mathbf{R}') - \phi + \theta_{\mathbf{k}}\}} w_{-,s}^a w_{-,s}^b e^{-i\theta_{\mathbf{k}}} (-a(\mathbf{R})b(\mathbf{R}') + b(\mathbf{R})a(\mathbf{R}')) \right\} \end{aligned} \quad (\text{E23})$$

1298 We note that $w_{-,s}^a w_{-,s}^b = -w_{+,s}^a w_{+,s}^b$, and is independent of spin index s . Performing the summation over \mathbf{k}

$$\int w_{+,s}^a w_{+,s}^b \Delta_k e^{i\mathbf{k}\cdot(\mathbf{R}-\mathbf{R}')} \frac{d^2\mathbf{k}}{(2\pi)^2} = \int \frac{vk}{\varepsilon_{\mathbf{k}}} \Delta_k J_0(k|\mathbf{R}-\mathbf{R}'|) \frac{kdk}{2\pi} = f_0^{AB}(|\mathbf{R}-\mathbf{R}'|) \quad (\text{E24})$$

1299 we find

$$\begin{aligned} \Delta(\mathbf{R}, \mathbf{R}') &= \frac{1}{2} f_0^{AB}(|\mathbf{R}-\mathbf{R}'|) \left[e^{i\{\mathbf{K}\cdot(\mathbf{R}+\mathbf{R}')+\phi\}} - e^{i\{-\mathbf{K}\cdot(\mathbf{R}+\mathbf{R}')-\phi\}} \right] [-a(\mathbf{R})b(\mathbf{R}') + b(\mathbf{R})a(\mathbf{R}')] \\ &= i f_0^{AB}(|\mathbf{R}-\mathbf{R}'|) [\sin(\mathbf{K}\cdot(\mathbf{R}+\mathbf{R}')+\phi)] [-a(\mathbf{R})b(\mathbf{R}') + b(\mathbf{R})a(\mathbf{R}')], \end{aligned} \quad (\text{E25})$$

1300 and therefore, with $\mathbf{R} \in A, \mathbf{R}' \in B$,

$$H_{\Delta} = \sum_{\langle \mathbf{R}, \mathbf{R}' \rangle} \Delta' \left[\sin(\mathbf{K}\cdot(\mathbf{R}+\mathbf{R}')+\phi) c_{\mathbf{R}}^{\dagger} c_{\mathbf{R}'}^{\dagger} + \text{h.c.} \right]. \quad (\text{E26})$$

1301 where $\Delta' = i f_0^{AB}(|\mathbf{R}-\mathbf{R}'|)$.